UC Irvine
UC Irvine Electronic Theses and Dissertations

Title
Third Order Exceptional Point of Degeneracy in Coupled Optical Waveguide

Permalink
https://escholarship.org/uc/item/0187s6q7

Author
Furman, Nathaniel

Publication Date
2022

Peer reviewed|Thesis/dissertation

UNIVERSITY OF CALIFORNIA,
IRVINE

Third Order Exceptional Point of Degeneracy in Coupled Optical Waveguide

THESIS

Submitted in partial satisfaction of the requirements
for the degree of

MASTER OF SCIENCE

in Electrical Engineering and Computer Science

by

Nathaniel Furman

Thesis Committee:
Professor Filippo Capolino, Chair
Associate Professor Ozdal Boyraz
Associate Professor Maxim Shcherbakov

2022

TABLE OF CONTENTS

LIST OF FIGURES

ACKNOWLEDGEMENTS

I extend my thanks and gratitude to my advisor and thesis committee chair Dr. Filippo Capolino. Through his patience and support, I have been able to make the most of my opportunity to work with him and his research group. This thesis is possible because of his attention to detail and the care taken to develop fundamental understandings of our work.

I also would like to thank my colleagues Tarek Mealy, Robert Marosi, and Albert Herrero Parareda for their valuable thoughts and inputs. Through multiple fruitful discussions I was able to further understand and consider important points about optical waveguides and exceptional points of degeneracy.

ABSTRACT OF THE THESIS

Third Order Exceptional Point of Degeneracy in Coupled Optical Waveguide

By

Nathaniel Furman

Master of Science in Electrical Engineering and Computer Science

University of California, Irvine, 2022

Professor Filippo Capolino, Chair

The field of exceptional points of degeneracy (EPDs) has seen a resurgence in research over the past few decades as theory and practice have coalesced into a better understanding of system behavior along with experimental verifications. Researchers have considered applications in high-sensitivity sensors, optical delay lines, lasers, and more. Each structure, from a combination of model parameters and boundary conditions, supports an EPD. An EPD is a special point in the transfer matrix describing the relationship between the input and output electromagnetic fields where multiple eigenmodes coalesce in both their eigenvalues and eigenvectors. This thesis proposes an optical waveguide (OWG) structure and design containing both coupling between waveguides and reflection in the OWG using a distributed Bragg reflector. We validate the existence of the EPD by examining the behavior of the system through numerical methods and examine properties of the transfer function in a finite length structure.

INTRODUCTION

1.1 Exceptional Points of Degeneracy

Before discussing optical wave guide (OWG) modeling and geometries, exceptional points of degeneracy (EPDs) must first be understood and discussed. We begin with a formalism discussed in [1], [2] where the transfer matrix describing the evolution of a given state vector across a given period experiences eigenmodes where the corresponding eigenvectors and eigenvalues have a modal degeneracy of order two or greater [3]–[7]. This multiplicity in the eigenvalues is an emergent behavior based on system configurations and parameters. In general, this multiplicity can be adjusted based on design requirements.

We also clarify here the differences in nomenclature from diabolical points, exceptional points, and exceptional points of degeneracy. Other fields, particularly physics, may generalize an exceptional point for a variety of important phenomena based on the current model or analysis. We add the "D" in EPD as "degeneracy" to specify the kind of exceptional points we describe and engineer. Diabolical points are the points occuring in Hermitian systems and differ from EPDs in that only the eigenfrequencies coalescence at a diabolical point where the eigenfrequencies and the eigenstates must coalesce in an EPD topology. As discussed thoroughly in [3], [6], [8], EPDs occur in non-Hermitian systems. As such, our analysis and discussion will not include diabolical points.

The second order degeneracy is commonly referred to as the regular band edge (RBE). A classic example of the RBE is the frequency cutoff point in a waveguide [9], [10]. Below the cutoff, only evanescent or purely imaginary modes propagate, where at the cutoff the eigenmodes split into purely real modes for a lossless waveguide. Traditionally, the RBE has not been included in

1

EDP discussions because of its common nature and closer association with transmission line theory. Although the RBE has important applications in single-mode operation conditions and frequency splitting [11], [12], we will not discuss this degeneracy further.

The fourth order degeneracy, or the degenerate band edge (DBE), is another exceptional point important to a variety of lasers, sensors, and more [1], [10], [13]–[19]. The DBE will not be discussed in this thesis.

The remainder of this thesis investigates the third order degeneracy, or stationary inflection point (SIP). As will be detailed further later, the SIP occurs when three forward propagating and three backward propagating eigenmodes have equal eigenvectors and propagate through the waveguide with the same eigenvalues. This formalism will be further discussed in Sec. 2.5. We briefly note the impact of parity-time (*PT)* symmetric systems in EPD behavior and existence. Generally, EPDs are contingent upon *PT* symmetric systems, yet this is not required for all EPDs [8], [20]–[29].

1.2 Motivation

The SIP has important properties when analyzed in an isolated environment and when analyzed with respect to other EPDs. This section first details important general aspects of the SIP before addressing differences between the SIP and other EPDs.

Under the umbrella of integrated photonic devices, EPDs in the optical regime can give rise to improvements in novel and niche computing systems, in data transmission and communication systems, in extremely sensitive sensors, and more [2], [30], [31]. Using unconventional quality factor scaling and group velocity properties, devices operating at an EPD can obtain significant improvements to energy consumption, mode discrimination, and overall efficiency. The ability to

engineer the modal behavior inside a photonic structure, particularly around an EPD, allows for higher performance photonic devices and cavities. EPDs are also generally very sensitive to variations in system parameters. With less than a percent change in any given geometric value describing the system configuration, the EPD devolves into multiple eigenvalues with similar values rather than multiple perfectly coalescing eigenvalues. We can use this behavior to design sensors with sensitivity orders of magnitude finer than non-EPD based designs.

More specific to the SIP, this point does not necessarily have a photonic bandgap in the dispersion diagram. Directional propagation is also maintained with frequencies above and below the SIP frequency. These properties, along with a near-zero group velocity dispersion (GVD) at the SIP, make for excellent photonic delay lines [4], [18], [32]. Increasing the delay while maintaining a small footprint and minimal signal dispersion are the key elements for all-optical routers in fiber communication systems.

Along with delay lines, a monotonic slope in the real dispersion wavenumber around the SIP may provide significant improvements in lasing. A combination of near-zero GVD and monotonic dispersion slope help facilitate strong light-matter interactions. High output gain may be achieved in a smaller waveguide system operating at the SIP [2], [16], [30], [33]–[44].

While EPDs, and specifically the SIP, are still actively being investigated and researched, the possible applications and improvements to current photonic systems are clear and important. By studying and describing more geometries which support the SIP, we hope to further develop this field and motivate more investigation into SIP devices.

1.3 Analyzing Methods

When analyzing and modeling various waveguide geometries, and more generally system behavior, two methods are critically important: the transfer matrix method and the scattering matrix method. Each of these two methods have distinct advantages over the other, and relationships between the methods can readily be developed. In this section, we will start with a simple definition of a two-port network with incident and reflected wave amplitudes described by $\underline{\mathbf{a}}$ and $\underline{\mathbf{b}}$, and subscripts used for denoting the input (1) side and output (2) side. Later sections of this thesis will explore the meaning and arrangement of various system matrix definitions based on physical properties.

We start by describing the scattering matrix method with a form given by (1.3.1). This matrix describes how the reflected fields respond to given incident fields when terminated by an impedance. If another impedance terminates the network, a conversion must be calculated as performed in [45], [46]. For simplicity, the scattering parameters will be given with respect to the characteristic impedance of an unloaded, unperturbed waveguide. This characteristic impedance will in general be frequency dependent and dependent on the geometry of the waveguide.

$$\begin{pmatrix} \mathbf{b}_1 \\ \mathbf{b}_2 \end{pmatrix} = \begin{pmatrix} \underline{\underline{\mathbf{S}}}_{11} & \underline{\underline{\mathbf{S}}}_{12} \\ \underline{\underline{\mathbf{S}}}_{21} & \underline{\underline{\mathbf{S}}}_{22} \end{pmatrix} \begin{pmatrix} \mathbf{a}_1 \\ \mathbf{a}_2 \end{pmatrix}, \qquad \mathbf{b} = \underline{\underline{\mathbf{S}}}\,\underline{\mathbf{a}} \tag{1.3.1}$$

In this sample two-port network, we can describe three key conditions of the scattering matrix: reciprocal, symmetric, and lossless. For a reciprocal network, an outside observer must not be able to tell the difference in transmitted signals between two networks where one of the networks has had its ports reversed with respect to the other. In mathematical formulation, the condition for reciprocity is written as $\underline{\underline{\mathbf{S}}}_{ij} = \underline{\underline{\mathbf{S}}}_{ji}$. As an incident signal is applied from either side of the network, the transmitted signal behaves the same regardless of the chosen input port. In symmetric

4

networks, a similar condition applies to the diagonal entries of the scattering matrix. For a symmetric network, an outside observer must not be able to tell the difference in reflected signals between two networks where one of the networks' ports were reversed with respect to the other. Thus, the condition is written as $\underline{\underline{\mathbf{S}}}_{ii} = \underline{\underline{\mathbf{S}}}_{jj}$.

For a lossless network, the energy input into the network must equal the energy output from the network. With $\underline{\mathbf{a}}$ and $\underline{\mathbf{b}}$ describing incident and reflected complex electric field amplitudes, the power out is given by (1.3.2) where '†' represents the complex conjugate transpose (or Hermitian conjugate) operation. Substituting the relationship between $\underline{\mathbf{a}}$ and $\underline{\mathbf{b}}$ as the scattering matrix itself and distributing the Hermitian conjugate operation, we arrive at (1.3.3). As a parallel to (1.3.2), we also write the input power based on the incident signal in a similar manner. To achieve a lossless network, therefore, the scattering matrix must be unitary, or $\underline{\underline{\mathbf{S}}}\,\underline{\underline{\mathbf{S}}}^{\dagger} = \underline{\underline{\mathbf{I}}}$ where $\underline{\underline{\mathbf{I}}}$ is the identity matrix.

$$P_{out} = \underline{\mathbf{b}}\,\underline{\mathbf{b}}^{\dagger}, \quad \underline{\mathbf{b}} = \begin{bmatrix} \underline{\mathbf{b}}_1, & \underline{\mathbf{b}}_2 \end{bmatrix} \tag{1.3.2}$$

$$P_{out} = \underline{\mathbf{a}}(\underline{\underline{\mathbf{S}}}\,\underline{\underline{\mathbf{S}}}^{\dagger})\underline{\mathbf{a}}^{\dagger} \tag{1.3.3}$$

The scattering matrix is useful when describing a singular network or a singular block of a network. This matrix has uses in signal flow graphs and simplifying related calculations. The scattering matrix is also generally defined with respect to a reference plane. The conversion between reference planes is commonly documented as in [45], [46]. While this matrix has its applications and uses, it has drawbacks in cascaded systems with multiple network blocks.

The transfer matrix is primarily useful when combining multiple system blocks with clearly defined input and output ports. Instead of describing the relationship between reflected and incident signals, the transfer matrix describes the relationship between input and output signals.

We make a point here regarding the forward and backward transfer matrix. Various books and articles describe different types of transfer matrices, including the T matrix and ABCD matrix. While the particular definition may be more useful for one application or another, this thesis uses a modified definition presented in (1.3.4) where the input signal is acted upon to calculate the output signal. This is commonly referred to as the forward transfer matrix as opposed to the ABCD matrix where the output signal is acted upon to calculate the input. In this equation, $\mathbf{\Psi'}$ represents the state vector and will be defined in later sections.

$$\begin{pmatrix} \mathbf{b}_2 \\ \mathbf{a}_2 \end{pmatrix} = \begin{pmatrix} \underline{\underline{\mathbf{T}}}_{11} & \underline{\underline{\mathbf{T}}}_{12} \\ \underline{\underline{\mathbf{T}}}_{21} & \underline{\underline{\mathbf{T}}}_{22} \end{pmatrix} \begin{pmatrix} \mathbf{a}_1 \\ \mathbf{b}_1 \end{pmatrix}, \qquad \mathbf{\Psi'}_2 = \underline{\underline{\mathbf{T}}} \, \mathbf{\Psi'}_1 \tag{1.3.4}$$

Similar to the scattering matrix, we can define the same three conditions for the transfer matrix. For brevity, the conditions will be summarized and based on definitions given in [47]. For Lorentz reciprocity, the transfer matrix behaves as $\underline{\underline{\mathbf{T}}}^T \underline{\underline{\mathbf{l}}} \, \underline{\underline{\mathbf{T}}} = \underline{\underline{\mathbf{l}}}$ where $\underline{\underline{\mathbf{l}}}$ is defined in (1.3.5).

$$\underline{\underline{\mathbf{l}}} = \frac{1}{2j} \begin{pmatrix} \mathbf{0} & -\mathbf{1} \\ +\mathbf{1} & \mathbf{0} \end{pmatrix} \tag{1.3.5}$$

For a symmetric system, the transfer matrix behaves as $\underline{\underline{\mathbf{T}}} = \underline{\underline{\mathbf{r}}} \, \underline{\underline{\mathbf{T}}}^{-1} \underline{\underline{\mathbf{r}}}$ where $\underline{\underline{\mathbf{r}}}$ is defined in (1.3.6).

$$\underline{\underline{\mathbf{r}}} = \begin{pmatrix} \mathbf{0} & \mathbf{1} \\ \mathbf{1} & \mathbf{0} \end{pmatrix} \tag{1.3.6}$$

Finally, for a lossless system, the transfer matrix behaves as $\underline{\underline{\mathbf{T}}}^\dagger \underline{\underline{\mathbf{p}}} \, \underline{\underline{\mathbf{T}}} = \underline{\underline{\mathbf{p}}}$ with $\underline{\underline{\mathbf{p}}}$ defined in (1.3.7).

$$\underline{\underline{\mathbf{p}}} = \begin{pmatrix} +\mathbf{1} & \mathbf{0} \\ \mathbf{0} & -\mathbf{1} \end{pmatrix} \tag{1.3.7}$$

This forward transfer matrix and the generalized scattering matrix can be used to describe the same network. As such, it is useful to describe the transformation between these two

representations. Equations (1.3.8) and (1.3.9) describe the transformation from the scattering to the transfer matrix and from the transfer matrix to the scattering matrix, respectively. In the formulations presented, each sub-block of the full transfer or scattering matrix can represent another matrix for more than two port networks.

$$
\begin{aligned}
&\underline{\underline{S}}_{11} = -\underline{\underline{T}}_{22}^{-1}\underline{\underline{T}}_{21}, \quad \underline{\underline{S}}_{12} = \underline{\underline{T}}_{22}^{-1}, \\
&\underline{\underline{S}}_{21} = \underline{\underline{T}}_{11} - \underline{\underline{T}}_{12}\underline{\underline{T}}_{22}^{-1}\underline{\underline{T}}_{21}, \\
&\underline{\underline{S}}_{22} = \underline{\underline{T}}_{12}\underline{\underline{T}}_{22}^{-1}
\end{aligned}
\tag{1.3.8}
$$

$$
\begin{aligned}
&\underline{\underline{T}}_{11} = \underline{\underline{S}}_{21} - \underline{\underline{S}}_{22}\underline{\underline{S}}_{12}^{-1}\underline{\underline{S}}_{11}, \\
&\underline{\underline{T}}_{12} = \underline{\underline{S}}_{22}\underline{\underline{S}}_{12}^{-1}, \quad \underline{\underline{T}}_{21} = -\underline{\underline{S}}_{12}^{-1}\underline{\underline{S}}_{11}, \\
&\underline{\underline{T}}_{22} = \underline{\underline{S}}_{12}^{-1}
\end{aligned}
\tag{1.3.9}
$$

1.4 Organization of this Thesis

The remainder of this thesis details first how we model the OWG using a transfer matrix analysis. Each subblock of the system is described along with how the transfer matrix of the entire unit cell is constructed. Care is taken to describe the distributed Bragg reflector (DBR) modeling and how to incorporate electromagnetic field solver results into an analytic transfer matrix method model. We also detail the modeling of a distributed directional coupler in terms of even and odd modes and how to convert to a more useful state vector representation for our analysis.

The dispersion diagram of the unit cell structure is then described and shown in the context of Floquet-Bloch periodic structure theory. Multiple representations of the dispersion relation are shown that highlight various points important to understanding the structure's behavior. Using the eigenvectors of the unit cell structure, we present a key figure of merit called the coalescence parameter to describe how close the system operates to the SIP.

We finally analyze the finite length structure for a given number of unit cells N using proper boundary conditions. The transfer function is used to calculate the group delay at the SIP resonance frequency and the quality factor of the structure. We present a trend in the group delay as the number of unit cells increase.

THIRD ORDER EXCEPTIONAL POINT WAVEGUIDE

2.1 Outline and Subsections of Geometry

To engineer and observe SIP behavior, we must first model the unit cell of the system and individual elements of the system. This section gives proper form to **a** and **b** for the transfer and scattering matrices and describes the state vector used in modeling system elements. We also describe a second state vector useful when converting between scattering and transfer matrices, as well as converting between state vector representations. This section will finally describe the phase delay and directional coupling scattering and transfer matrices while the next section will describe the distributed Bragg reflector.

We start with the description of a z-direction traveling electromagnetic wave in the form $\vec{E}_n(z,t) = \mathrm{Re}\{\underline{\mathbf{a}}_n e^{j(\omega t - k_n z)} + \underline{\mathbf{b}}_n e^{j(\omega t + k_n z)}\}$ with the overbar arrow signifing that the time convention is included. More simply, we write $\mathbf{E}_n(z) = \left[E_n^+(z), \quad E_n^-(z) \right]^T$ with the $e^{j\omega t}$ time convention assumed, the superscript '*T*' representing the transpose operation, and the subscript '*n*' representing the port. In this description, the total electric field is a combination of the forward propagating and backwards propagating components of the electric field. Using this notation, we write the state vector for our six-port network in (2.1.1) and geometry shown in <u>Fig. 1</u>.

$$\Psi(z) = \begin{pmatrix} \mathbf{E}_1(z) \\ \mathbf{E}_2(z) \\ \mathbf{E}_3(z) \end{pmatrix} \tag{2.1.1}$$

This definition of the state vector groups the electric fields by the primary waveguides in which they are propagating rather than grouping the fields by the forwards and backwards directions of propagation. This secondary state vector is described by $\Psi'(z) = \left(\mathbf{E}^+(z), \quad \mathbf{E}^-(z) \right)^T$ where

9

$\mathbf{E}^+(z) = \begin{bmatrix} E_1^+(z), & E_2^+(z), & ... & E_n^+(z) \end{bmatrix}^T$ in general for N ports and similarly for the backwards

propagating waves.
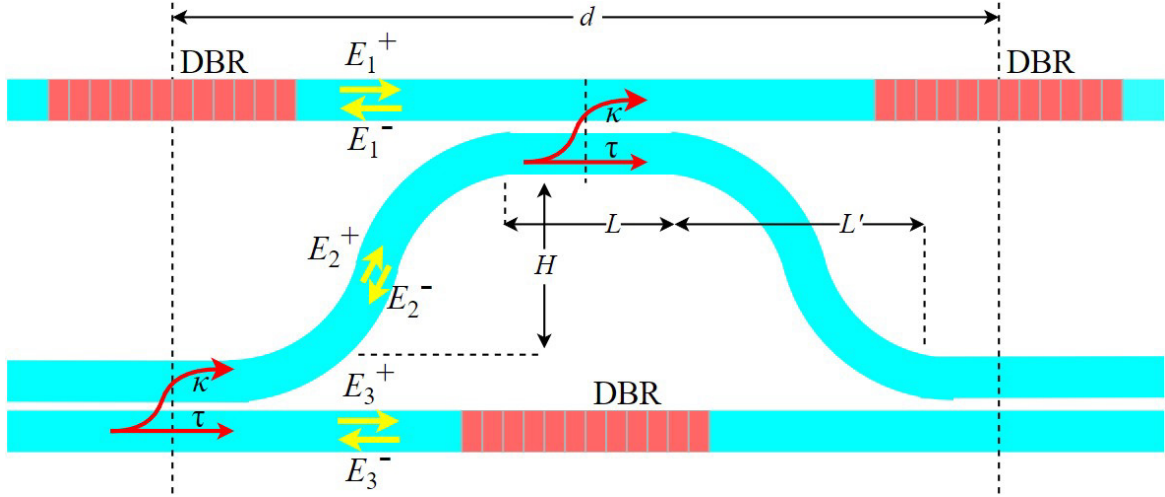
(a)
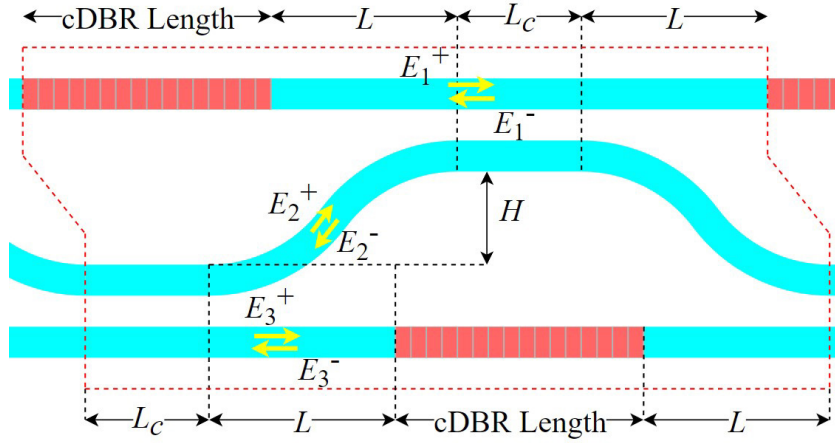
(b)

Figure 1. (a) Geometry of a single unit cell with period $d = 2(L + L')$ for the point coupling model. (b) Geometry of a single unit cell with period $d = 2L + L_{cDBR} + L_c$ for the distributed coupling model. The figure shows the directional coupler and the distributed Bragg reflector along with the orientation of the electric field amplitudes corresponding to the three waveguides.

Using the state vector in (2.1.1), we can write the relationship between a point z_1 and z_2 in

the network as

$$\mathbf{\Psi}(z_2) = \underline{\mathbf{T}}(z_2, z_1)\mathbf{\Psi}(z_1) \tag{2.1.2}$$

where $\underline{\mathbf{T}}(z_2, z_1)$ is the forwards transfer matrix from z_1 to z_2. In the context of a unit cell in the periodic structure of length d, we can write

$$\mathbf{\Psi}(z+d) = \underline{\mathbf{T}}_U\mathbf{\Psi}(z) \tag{2.1.3}$$

where $\underline{\mathbf{T}}_U$ is the transfer matrix for one unit cell. This formalism and methodology are similar to those presented in [1], [17], [18], [48]–[51]. We can also convert between transfer matrices describing the evolution of $\mathbf{\Psi}$ and $\mathbf{\Psi}'$ using (2.1.4) below.

$$\underline{\mathbf{T}}' = \underline{\mathbf{A}}\underline{\mathbf{T}}\underline{\mathbf{A}}^{-1} \tag{2.1.4}$$

For a six port network, $\underline{\mathbf{A}}_6$ is defined as

$$\underline{\mathbf{A}}_6 = \begin{pmatrix} 1 & 0 & 0 & 0 & 0 & 0 \\ 0 & 0 & 1 & 0 & 0 & 0 \\ 0 & 0 & 0 & 0 & 1 & 0 \\ 0 & 1 & 0 & 0 & 0 & 0 \\ 0 & 0 & 0 & 1 & 0 & 0 \\ 0 & 0 & 0 & 0 & 0 & 1 \end{pmatrix} \tag{2.1.5}$$

Similarly, a four-port network transfer matrix transformation has $\underline{\mathbf{A}}_4$ defined as

$$\underline{\mathbf{A}}_4 = \begin{pmatrix} 1 & 0 & 0 & 0 \\ 0 & 0 & 1 & 0 \\ 0 & 1 & 0 & 0 \\ 0 & 0 & 0 & 1 \end{pmatrix} \tag{2.1.6}$$

Converting the opposite direction uses the same definitions of $\underline{\mathbf{A}}$ and reversing (2.1.4) as

$$\underline{\mathbf{T}} = \underline{\mathbf{A}}^{-1}\underline{\mathbf{T}}'\underline{\mathbf{A}} \tag{2.1.7}$$

It is critically important to note that the equations describing the conversion between transfer and scattering matrices is contingent upon using $\mathbf{\Psi}'$ instead of $\mathbf{\Psi}$ for more than two-port networks. This is entirely due to the grouping of electric field amplitudes by direction rather than

11

port. Equivalent equations for conversion between transfer and scattering matrices for higher number port networks are possible yet are more complicated.

When modeling the propagation of a signal in a linear isotropic media without gain or loss, the signal experiences only a phase delay dependent on the length of the waveguide and the effective refractive index seen by the signal in the waveguide. The phase delay for a forward propagating wave over a given length x can thus be described by $\Omega_{w+} = e^{-jk_w x}$ where $k_w = n_w k_0$. In this equation k_0 represents the free space wavenumber, n_w is the effective refractive index or the modal index in the waveguide, and k_w is the propagation wavenumber in the waveguide. The phase delay for a backwards propagating wave is written in the same form with a positive exponent. In general, n_w is geometry and material dependent. For our system, we are modeling a waveguide with a cross section of dimensions $h = 220$ nm and $w = 450$ nm as shown in Fig. 2. Silicon dioxide cladding with a refractive index $n_{SiO_2} = 1.45$ is used around the silicon core. We use a standard refractive index value for Silicon of $n_{Si} = 3.476$. These values give an approximate modal refractive index of $n_w = 2.351$ at 193 THz. The phase delay transfer matrix can finally be written as

$$\underline{\mathbf{T}}_{phase} = \begin{pmatrix} \Omega_{w+} & 0 \\ 0 & \Omega_{w-} \end{pmatrix} \qquad (2.1.8)$$
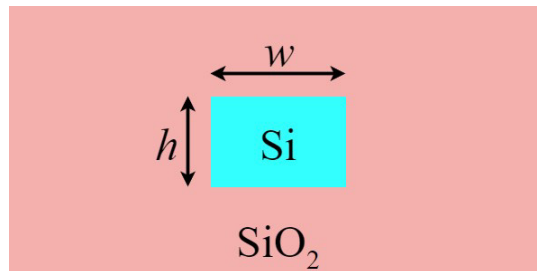
Figure 2. General description of the silicon core-cladding waveguide.

For the directional coupler, it is first useful to write the scattering matrix describing the relationship between incident and reflected electric field amplitudes as (2.1.9) where τ_c, κ represent the transmission and coupling coefficients, respectively. We assume real values for τ_c and κ without a loss of generality and that the coupling is lossless, or $\tau_c^2 + \kappa^2 = 1$ [52], [53]. We use both notations for the electric field amplitudes to explicitly demonstrate the usefulness of the two state vector definitions and the conversion between them.

$$
\begin{pmatrix} b_1(z_1) \\ b_2(z_1) \\ b_1(z_2) \\ b_2(z_2) \end{pmatrix} = \underline{\mathbf{S}}_{couple} \begin{pmatrix} a_1(z_1) \\ a_2(z_1) \\ a_1(z_2) \\ a_2(z_2) \end{pmatrix}, \quad \begin{pmatrix} E_1^-(z_1) \\ E_2^-(z_1) \\ E_1^+(z_2) \\ E_2^+(z_2) \end{pmatrix} = \underline{\mathbf{S}}_{couple} \begin{pmatrix} E_1^+(z_1) \\ E_2^+(z_1) \\ E_1^-(z_2) \\ E_2^-(z_2) \end{pmatrix}, \quad \underline{\mathbf{S}}_{couple} = \begin{pmatrix} 0 & 0 & \tau_c & j\kappa \\ 0 & 0 & j\kappa & \tau_c \\ \tau_c & j\kappa & 0 & 0 \\ j\kappa & \tau_c & 0 & 0 \end{pmatrix}
$$

$$(2.1.9)$$

Before converting directly to the transfer matrix describing the evolution of $\boldsymbol{\Psi}$, we must first use the transformation of the scattering to transfer matrix in (1.3.8) where the transfer matrix describes the evolution of $\boldsymbol{\Psi}'$. This $\underline{\mathbf{S}} \to \underline{\mathbf{T}}'$ transformation gives a transfer matrix

$$
\underline{\mathbf{T}}'_{couple} = \begin{pmatrix} \tau_c & j\kappa & 0 & 0 \\ j\kappa & \tau_c & 0 & 0 \\ 0 & 0 & \tau_c & -j\kappa \\ 0 & 0 & -j\kappa & \tau_c \end{pmatrix} \tag{2.1.10}
$$

To finally arrive at our intended transfer matrix describing $\boldsymbol{\Psi}(z_2) = \underline{\mathbf{T}}_{couple}\boldsymbol{\Psi}(z_1)$, we apply (2.1.7) and write the transfer matrix as

$$
\underline{\mathbf{T}}_{couple} = \begin{pmatrix} \tau_c & 0 & j\kappa & 0 \\ 0 & \tau_c & 0 & -j\kappa \\ j\kappa & 0 & \tau_c & 0 \\ 0 & -j\kappa & 0 & \tau_c \end{pmatrix} \tag{2.1.11}
$$

We perform three checks for the scattering and transfer matrices described in this section: lossless, reciprocal, and symmetric. It is clear that the scattering matrices are symmetric and

reciprocal, and easy to demonstrate they are unitary once the lossless condition is applied. Some care must be taken when using (1.3.9) for the four-port transfer matrix. As shown in (1.3.4), the conditions of the transfer matrix are written with the field amplitudes grouped by propagation direction rather than by port. Thus, $\underline{\mathbf{T}}'_{couple}$ must be used instead of $\underline{\mathbf{T}}_{couple}$.

2.2 Modeling a Distributed Bragg Reflector

Similar to modeling the directional coupler, we start with the scattering matrix when describing the distributed Bragg reflector, or DBR. The primary concept of any DBR is using constructive and destructive interference to selectively reflect specific wavelengths in a waveguide. Many dielectric DBR designs are made for high reflectivity (> 99.5%) [31], [52]–[56], yet our requirements are less restrictive. Our design should provide a modest field reflection coefficient at 193 THz (~1550 nm) and minimize losses due to scattering, mode mismatch, and more.
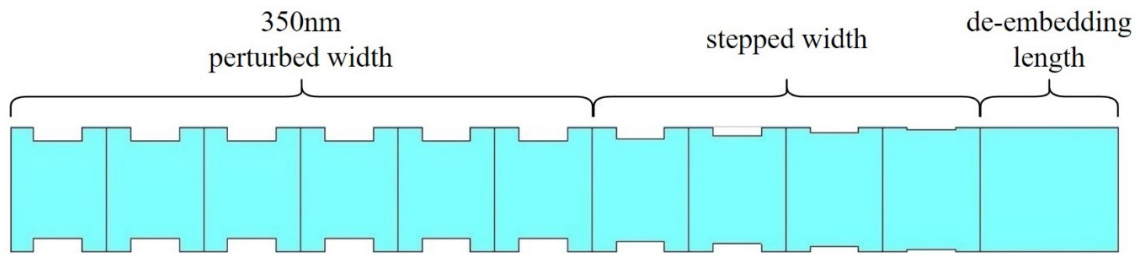
Figure 3. Half of the chirped distributed Bragg reflector with key sections highlighted.

Generally, the period between high and low refractive index materials is a quarter of the wavelength, or ~380 nm. Our initial design selects a period of 350 nm and a duty cycle of 50% between perturbed and unperturbed widths in the waveguide. We also choose a difference between the unperturbed waveguide width and the perturbed waveguide width of 50 nm on each side, or a total width of 350 nm. The waveguide height is not changed. Increasing this difference increases the size of the effective index variation and thus the magnitude of the reflection coefficient.

14

However, there is a tradeoff between the perturbation size and losses. With a larger disconnect, more power will be scattered away from the waveguide and increase losses in the system. The last initial design choice is the number of unit cells in the DBR. The more unit cells, the stronger the interference and the larger the reflection coefficient at the expense of a larger system. We choose 10 unit cells initially and perform a full-wave simulation using CST Studio Suite.

After plotting the loss in the DBR described by (2.2.1), we notice losses are too significant when cascading multiple full unit cell structures together. In this equation, S_{22} and S_{21} can be used interchangeably with S_{11} and S_{12} as the DBR is symmetric and reciprocal. The normalization impedance is also arbitrary when using this formula as the scattering parameters are not yet analyzed with respect to the overall structure.

$$L_{dB} = -10\log(|S_{11}|^2 + |S_{12}|^2)$$
(2.2.1)
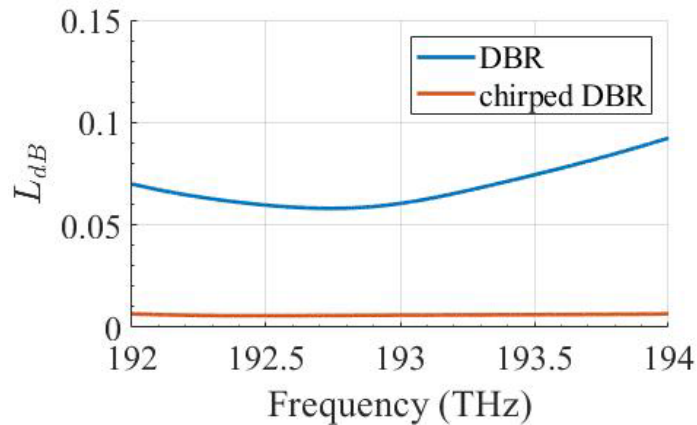
Figure 4. dB loss calculations from CST Studio Suite for the DBR and cDBR designs.

We now modify our design from a DBR to a chirped DBR, or cDBR. One of the defining characteristics of a cDBR is varying the perturbed waveguide width gradually from 450 nm (unperturbed) to 350 nm (fully perturbed). There can be significant tradeoffs between the number of unit cells used to step the widths smaller and the losses in the cDBR. For our updated cDBR

design, we first step down from 450 nm in 20 nm increments over four periods. This is performed on each side of the DBR for a total of eight extra periods with gradually varying widths.

From the CST simulation of the cDBR, we effectively decrease the losses in the system significantly without greatly affecting the reflection coefficient around 193 THz. This is primarily because the signal in the waveguide does not experience a sharp reflection and scattering from a 450 nm to 350 nm jump and alternatively experiences multiple softer reflections as the signal propagates through the waveguide. While the cDBR provides an improved design over the DBR, we further minimized the loss by modifying the stepped widths. The current best design is shown in Fig. 3. This cDBR uses stepped widths of 430 nm, 400 nm, 375 nm, and 360 nm between the unperturbed 450 nm and repeating unit cell of 350 nm perturbed widths. At 193 THz, $|S_{11}| = 0.516$, $|S_{12}| = 0.856$, and $L_{dB} = 0.0027$, which is similar to the scattering parameters for the DBR but with an order of magnitude less loss.

Before including the cDBR in the overall structure, it is important to note waveguide impedance and scattering parameter renormalization. When connecting the cDBR to a regular waveguide with the same dimensions, the only reflection should be from the cDBR itself and not a waveguide mismatch or equivalently an impedance mismatch. When CST exports the frequency dependent scattering parameters, the values are generally all normalized to 50 Ω for convenience. To effectively incorporate the transfer matrix of the cDBR in an analytic formulation consistent with the previously defined phase delay and directional coupler transfer matrices, the scattering matrix from CST must be renormalized to the frequency dependent port impedance corresponding to the same waveguide dimensions used throughout the system. Renormalizing the scattering parameters is commonly documented in [45], [46], and has built-in implementations in many

software suites including MATLAB. Once the scattering matrix has been renormalized, the standard conversion between the scattering and transfer matrix is used as before.

We also use de-embedding in CST to filter out evanescent modes which are nonexistent in the infinite length structure from Floquet-Bloch theory. We move the port a sizable fraction of the wavelength away from the first cDBR perturbed width and let CST shift the scattering matrix reference plane back the equivalent length added. This length is arbitrary if the evanescent modes resulting from a width change in the waveguide have distance to decay.

For comparison and optimization purposes, we can also develop a model for the cDBR which is lossless. To start, we impose the reciprocal and symmetric conditions and write $S_{11} = S_{22} = \rho e^{j\theta_\rho}$, $S_{12} = S_{21} = \tau_0 e^{j\theta_\tau}$. To impose the lossless condition, we first consider the magnitude condition derived from the diagonal elements of the unitary matrix then the phase condition derived from the off-diagonal elements of the unitary matrix. The magnitude equation is written as $1 = S_{11}S_{22}^* + S_{21}S_{12}^* = |S_{11}|^2 + |S_{12}|^2 \rightarrow |S_{12}| = \sqrt{1 - |S_{11}|^2}$ or equivalently $\tau_0 = \sqrt{1 - \rho_0^2}$. The phase equation is written as $0 = S_{11}S_{21}^* + S_{12}S_{22}^*$ and using minimal algebraic simplification along with employing Euler's identity, we write $e^{j(\angle S_{11} - \angle S_{21})} = e^{j(\angle S_{12} - \angle S_{22} + \pi)}$. This can be equivalently represented as $\theta_\tau = \theta_\rho - \pi/2$. Thus, the complete lossless cDBR representation is

$$\mathbf{\underline{T}}_{reflection} = \frac{1}{\tau_0 e^{j\theta_\tau}} \begin{pmatrix} (\tau_0 e^{j\theta_\tau})^2 - (\rho_0 e^{j\theta_\rho})^2 & \rho_0 e^{j\theta_\rho} \\ -\rho_0 e^{j\theta_\rho} & 1 \end{pmatrix} \qquad (2.2.2)$$

2.3 Modeling the Coupled Waveguide

Not unlike a regular, straight, waveguide, where we describe the electric field propagation by the modal, or effective, refractive index, we can describe the field in coupled waveguides by the

even and odd modes. The motivation for analyzing and implementing a distributed coupled waveguide model when we have already described a point coupling model is for more accurate representations of physical systems. As is clear from Fig. 1, the middle waveguide couples to both the upper and lower waveguides over a given distance. While the point coupling model is an excellent proxy for physical behavior, a full and more accurate model of coupled waveguides is significantly more useful to employ in modeling the unit cell.

These coupled waveguide modes are characterized by the relative polarization of the electric field. In the even mode, the fields in the waveguides constructively add in the same polarization direction. Thus, we generally see a stronger field between the waveguides in the silicon dioxide cladding. Conversely, the odd modes have opposite polarization fields relative to the two waveguides and thus we generally see a weaker field in the cladding region. We can describe the even and odd field modes in terms of the individual electric field modes in each waveguide as

$$
\begin{aligned}
\mathbf{E}_{t,e}(x,y,z) &= V_1(z)\mathbf{e}_1(x,y) + V_2(z)\mathbf{e}_2(x,y) = V_e(z)\mathbf{e}_e(x,y) \\
\mathbf{E}_{t,o}(x,y,z) &= V_1(z)\mathbf{e}_1(x,y) - V_2(z)\mathbf{e}_2(x,y) = V_o(z)\mathbf{e}_o(x,y)
\end{aligned}
\tag{2.3.1}
$$

In (2.3.1), $\mathbf{e}_1$ and $\mathbf{e}_2$ represent the individual transverse waveguide electric field mode profiles whereas $\mathbf{e}_e$ and $\mathbf{e}_o$ represent the even and odd mode profiles, respectively. Fig. 5 illustrates an overlay of the even and odd mode field contour and polarization from a CST simulation. As expected, we see the even mode polarization states are matched with a substantial field in the gap between waveguides and opposite polarization states for the odd mode with minimal field in the gap.

Furthermore, we can describe the scattering matrix relating the incident and reflected even and odd mode fields as in (2.3.2) where Ω_e, Ω_o are defined shortly. We draw attention to two aspects of this scattering matrix: the diagonal terms are zero and the cross-coupling terms are zero. Intuitively, it may be surprising to see no interaction between even and odd modes.

18

$$\begin{pmatrix} b_e(z_1) \\ b_o(z_1) \\ b_e(z_2) \\ b_o(z_2) \end{pmatrix} = \underline{\mathbf{S}}_{eo} \begin{pmatrix} a_e(z_1) \\ a_o(z_1) \\ a_e(z_2) \\ a_o(z_2) \end{pmatrix}, \quad \begin{pmatrix} E_e^-(z_1) \\ E_o^-(z_1) \\ E_e^+(z_2) \\ E_o^+(z_2) \end{pmatrix} = \underline{\mathbf{S}}_{eo} \begin{pmatrix} E_e^+(z_1) \\ E_o^+(z_1) \\ E_e^-(z_2) \\ E_o^-(z_2) \end{pmatrix}, \quad \underline{\mathbf{S}}_{eo} = \begin{pmatrix} 0 & 0 & \Omega_e & 0 \\ 0 & 0 & 0 & \Omega_o \\ \Omega_e & 0 & 0 & 0 \\ 0 & \Omega_o & 0 & 0 \end{pmatrix} \quad (2.3.2)$$

However, since we are not currently describing individual fields in each waveguide, the even and

odd modes simply propagate through the coupled waveguides not unlike a given mode propagating

through a regular isolated waveguide. Additionally, since the scattering matrix is given with

respect to the characteristic even and odd mode impedances, all reflection coefficients are zero.

Or, in other words, there is purely the transmission of even and odd modes.

In calculating the transmission coefficients and thus the scattering matrix, we simplify by using

the same formulation as the forward propagating field term in (2.1.8). However, instead of using

the effective refractive index for an isolated waveguide, we use the effective refractive indices for

even and odd modes. The particular values are frequency dependent and are calculated using high

accuracy CST simulations. Implementing the same formulation, we write $\Omega_e = e^{-jn_e k_0 x}$ and

$\Omega_o = e^{-jn_o k_0 x}$ for a given length x where n_e and n_o represent the effective even and odd mode

refractive indices or equivalently modal indices.

While the even and odd mode representation is useful in various calculations, our analytic

model uses forward and backward waves in each waveguide. As such, we need to convert from

even and odd modes to individual waveguide mode profiles making use of the definitions stated

above. Before describing the transformation, we first describe the expected form the resulting

matrix will take. In the simplest representation, the magnitude of the distributed coupling transfer

matrix will be identical to the representation in (2.1.11) for point-like coupling. The transmission

coefficients will be along the diagonal terms and the coupling coefficients will be imaginary and

negative with respect to the forward and backward modes. The primary difference in using the

even and odd mode formulation is that the transmission coefficients will have a phase delay included directly related to the length of the coupled waveguides. Substituting the relationships between even/odd modes and forward/backward modes into a symbolic equation solver, we solve for the forward and backward modes at one end of the structure in both waveguides in terms of the scattering matrix parameters.

The resulting transfer matrix parameters are comprised of over ten terms each for the general case. However, we can simplify the transformation in the ideal case (scattering matrix diagonal terms are zero, cross coupling terms are zero). The resulting distributed coupling transfer matrix for individual waveguide modes based on the scattering matrix from even and odd modes is described as

$$\mathbf{T}_{couple,distributed} = \begin{pmatrix} \dfrac{S_{31}+S_{42}}{2} & 0 & \dfrac{S_{31}-S_{42}}{2} & 0 \\ 0 & \dfrac{S_{13}+S_{24}}{2S_{13}S_{24}} & 0 & \dfrac{S_{24}-S_{13}}{2S_{13}S_{24}} \\ \dfrac{S_{31}-S_{42}}{2} & 0 & \dfrac{S_{31}+S_{42}}{2} & 0 \\ 0 & \dfrac{S_{24}-S_{13}}{2S_{13}S_{24}} & 0 & \dfrac{S_{13}+S_{24}}{2S_{13}S_{24}} \end{pmatrix}$$

$$= \begin{pmatrix} \dfrac{\Omega_e+\Omega_o}{2} & 0 & \dfrac{\Omega_e-\Omega_o}{2} & 0 \\ 0 & \dfrac{\Omega_e+\Omega_o}{2\Omega_e\Omega_o} & 0 & \dfrac{\Omega_o-\Omega_e}{2\Omega_e\Omega_o} \\ \dfrac{\Omega_e-\Omega_o}{2} & 0 & \dfrac{\Omega_e+\Omega_o}{2} & 0 \\ 0 & \dfrac{\Omega_o-\Omega_e}{2\Omega_e\Omega_o} & 0 & \dfrac{\Omega_e+\Omega_o}{2\Omega_e\Omega_o} \end{pmatrix}$$

(2.3.3)

We compute the even and odd mode effective refractive indices from a high quality CST simulation of coupled waveguides with the same dimensions as the isolated waveguide ([Fig. 2](#)) and a 150 nm gap between the waveguides. This gap size is somewhat arbitrary and can be adjusted depending on fabrication tolerances, size constraints, and much more. A gap below 50 nm may provide more coupling in a shorter distance yet risks more fabrication error in physical models.

Conversely, a wider gap may help with physical model reproducibility yet requires a longer distance for the same coupling strength. Fig. 6 shows the CST generated plot of the port effective dielectric constant. Even modes are denoted with a one in parenthesis and odd modes a two for both ports. Fig. 7 illustrates the magnitude of the field coupling coefficient and phase of the transmission coefficient for a given coupler length.

While it may be difficult to verify the accuracy of the distributed coupled transfer matrix in terms of the lossless, reciprocal, and symmetric conditions in symbolic terms, we provide an example using numerical values for a 1 µm long coupler. We also compare the results to the CST scattering matrix transformed to the transfer matrix at 193 THz per (1.3.9) and the following analysis in that section. Using the analytic distributed coupler model and the proper effective even/odd mode refractive indices, we determine the analytic transfer matrix as

$$\underline{\mathbf{T}}_{DC,analytic} = \begin{pmatrix} 0.995\angle 173.1° & 0 & 0.103\angle 83.1° & 0 \\ 0 & 0.995\angle -173.1° & 0 & 0.103\angle -83.1° \\ 0.103\angle 83.1° & 0 & 0.995\angle 173.1° & 0 \\ 0 & 0.103\angle -83.1° & 0 & 0.995\angle -173.1° \end{pmatrix} \tag{2.3.4}$$

whereas the transfer matrix from CST is

$$\underline{\mathbf{T}}_{DC,CST} = \begin{pmatrix} 0.995\angle 173.3° & 0 & 0.103\angle 83.6° & 0 \\ 0 & 0.995\angle -173.3° & 0 & 0.103\angle -83.6° \\ 0.103\angle 82.99° & 0 & 0.995\angle 173.3° & 0 \\ 0 & 0.103\angle -83.0° & 0 & 0.995\angle -173.3° \end{pmatrix} \tag{2.3.5}$$

We note here, however, the zero terms in (2.3.5) are abbreviated to zero. Upon carrying out the simulation and necessary transformations, these terms were on the order of 10^{-4} or smaller. As expected, the analytic model near perfectly matches the simulation.

21

(a)

(b)
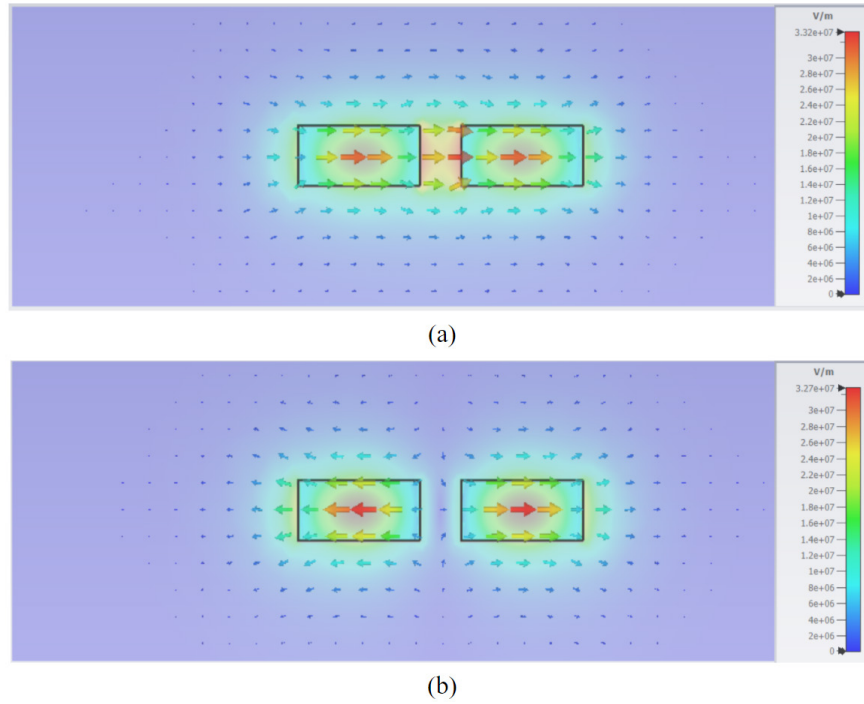
Figure 5. Even (a) and odd (b) electric field mode profiles from CST shown with the contour overlayed with the polarization arrows of the field.
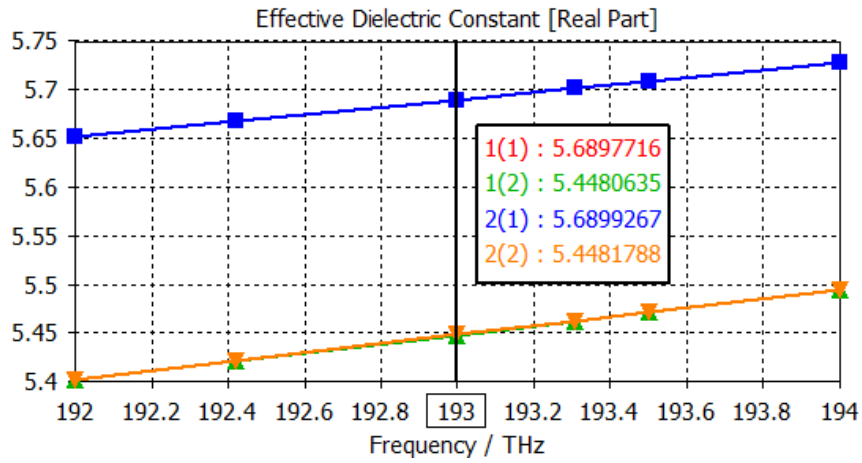
Figure 6. Effective dielectric constant of the even (1) and odd (2) modes for a coupled waveguide CST simulation with a 150 nm gap size.
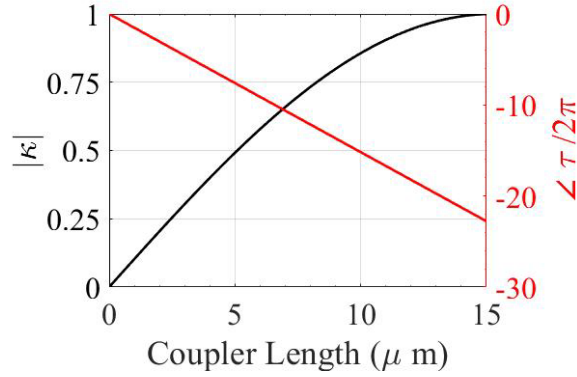
Figure 7. Magnitude of the field coupling coefficient and phase of the transmission coefficient for a distributed coupler of a given length and with a 150 nm gap size at 193 THz. Unitary coupling is achieved in 15 μm.

2.4 Modeling the Middle Waveguide Curve

In this section, we describe the geometric construction of the curved sections in the middle waveguide. Unlike designs at RF or in similar regimes, optical waveguides must make smooth transitions when changing propagating directions. The smaller the radius of the bend, generally the more losses the waveguide will incur. Additionally, as described in the distributed Bragg reflector section, changing the waveguide width will also incur more losses. Thus, in modeling the curved section, we have two primary goals: the curvature of the waveguide has a continuous slope, and the radius of curvature is maximized for given geometric parameters.

As is clear from observing of the unit cell structure, we can divide the curved section into four equivalent subsegments corresponding to two segments on the left and two on the right, each with a positive and negative concavity when taking the standard coordinate axis as a reference. As such, we only need to solve this problem once and mirror or translate the resulting arc through the unit cell. We will also take the center of our rectangular coordinate system as point *O* shown in Fig. 8. This point corresponds to the boundary where the straight waveguide transitions to the arc and the

23

center of the middle waveguide's width. We also mark point M which corresponds to half of the height and half of L' shown in Fig. 1(a). With minimal algebra, an equivalent point can be marked with the values defined in Fig. 1(b).
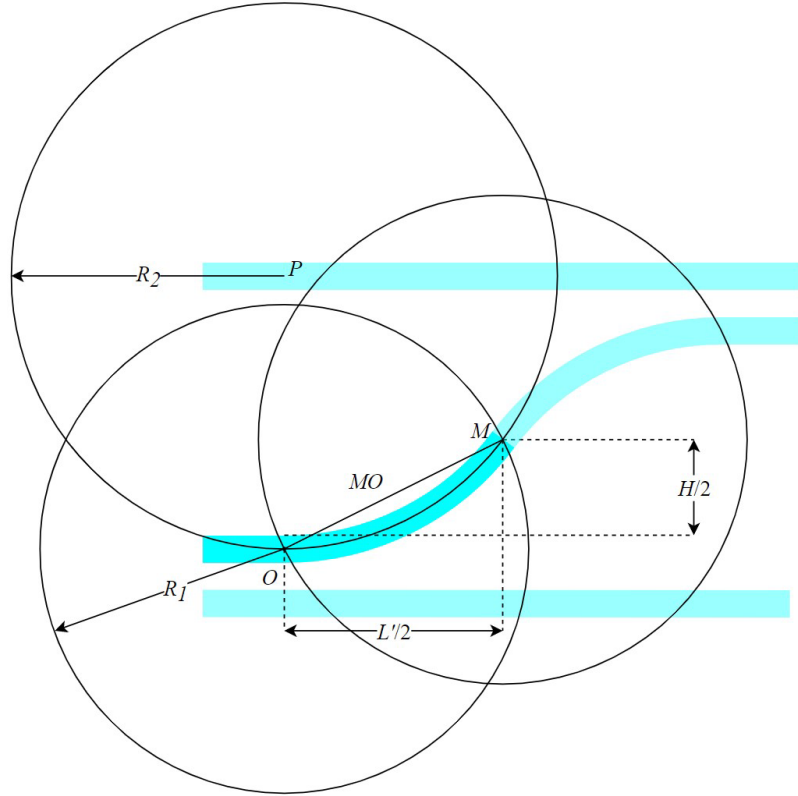
Figure 8. Geometric description of the bottom left middle curved waveguide arc.

In our formulation, line MO and radius R_1 are equivalent and are calculated using the Pythagorean theorem. We also know, to satisfy the maximum radius condition, the R_2 circle must have points O and M included on the perimeter. To ensure the arc's tangent at point O is always horizontal and thus satisfying the continuous curvature condition, we know the center of the R_2 circle must be directly above point O. We first write the general equation for the intersection of two circles described by the center point and radius as (x_1, y_1, R_1) and (x_2, y_2, R_2) in (2.4.1). By then setting the y-value intersection solution equal to the y-value of point M, we can solve for R_2.

Setting the initial x-values to zero and $y_1 = 0$, we simplify the solution to be solely dependent on H, w, and L', or the spacing of the middle waveguide, the width of the waveguides, and the distance of the curved section. This simplified formula is given in (2.4.2).

$$x_{center} = \frac{x_1 + x_2}{2} + \frac{R_1^2 - R_2^2}{2R^2}(x_2 - x_1) \pm \frac{1}{2}(y_2 - y_1)\sqrt{\frac{2(R_1^2 + R_2^2)}{R^2} - \frac{(R_1^2 - R_2^2)^2}{R^4} - 1}$$

$$y_{center} = \frac{y_1 + y_2}{2} + \frac{R_1^2 - R_2^2}{2R^2}(y_2 - y_1) \pm \frac{1}{2}(x_1 - x_2)\sqrt{\frac{2(R_1^2 + R_2^2)}{R^2} - \frac{(R_1^2 - R_2^2)^2}{R^4} - 1} \qquad (2.4.1)$$

$$R = \sqrt{(x_2 - x_1)^2 + (y_2 - y_1)^2}$$

$$R_2 = \frac{H^2 + 2Hw + w^2 + L'^2}{4(H + w)} \qquad (2.4.2)$$

As stated, the calculated radius R_2 is the same for every arc. The other three arcs can be constructed starting at the boundary between straight and curved sections, then drawing the appropriate circle either above or below the waveguide.

While it may seem unnecessary to detail the precise construction of these curved sections, it is critical to minimize losses in physical models. The formulation presented here also allows for a specific radius to be selected based on the height and length of the curve. This may be useful if fabrication tolerances allow for only specific radii, and the design can be quickly modified to ensure a minimum radius is not used.

2.5 Dispersion of the Eigenmodes

Before optimizing a design for the SIP, we must understand and solve the eigenvalue problem to find the modes of the infinite length unit cell. From Floquet-Bloch theory, periodic solutions to the eigenvalue problem given by (2.5.1) are in the form e^{-jkd} where k is the Floquet-Bloch complex wavenumber and where $\lambda \equiv e^{-jkd}$.

$$\underline{\mathbf{T}}_U \Psi = \lambda \Psi \qquad (2.5.1)$$

The eigenvalues λ_n with $n=1,2, ... 6$ are obtained by solving the characteristic equation $D(k,\omega) \equiv \det[\underline{\mathbf{T}}_U - \lambda \underline{\mathbf{1}}] = 0$ with $\underline{\mathbf{1}}$ representing the 6×6 identity matrix. Due to the reciprocity of the unit cell structure, the determinant of the unit cell transfer matrix satisfies the equation $\det[\underline{\mathbf{T}}_U] = 1$. Additionally, because we are working with a six port system, the eigenvalues will come in three sets of reciprocal pairs corresponding to the forwards and backwards directions of propagation. The dispersion diagram thus shows a symmetry such that if $k(\omega)$ is a solution of the eigenvalue equation, then $-k(\omega)$ is also a solution. Equivalently, the dispersion diagram is symmetric with respect to the center of the Brillouin Zone defined here with $\Re(k)$ from 0 to $2\pi/d$ where d is the length of the unit cell.

In this thesis, we present two models of the unit cell: one with point coupling and one with distributed coupling corresponding to Fig. 1(a) and Fig. 1(b), respectively. In turn, each of these two models are separated between the analytic and CST cDBR models. In the analytic version for the point coupling model, we use an ideal point reflection based on the CST cDBR parameters. Similarly, the analytic version for the distributed coupling model uses an ideal model of the reflection but accounts for the length of the cDBR as well. In the CST cDBR versions for both the point and distributed coupling models, the entire CST S-parameter file is used. Thus, in summary, the analytic models are perfectly lossless whereas the CST cDBR models account for the minimal losses associated with the reflecting structure.

We start with a description of the point coupling model. The full unit cell transfer matrix is calculated using a combination of the individual subblock matrices divided between five sections. The first section incorporates the cDBR block in the upper waveguide and the directional coupler between the bottom two waveguides. The second and fourth blocks are identical and describe the

phase delay in each of the waveguides as the middle waveguide curves between the upper and lower waveguides. The formulation for the arc length and geometric construction of the curved section is described in previous sections. The third block is similar to the first except the cDBR is in the lower waveguide and the directional coupler is between the middle and upper waveguide. The fifth block is simply a phase delay in each of the waveguides. We do not include the directional coupler or cDBR in the last subblock as to not account for these structures twice at the same location.
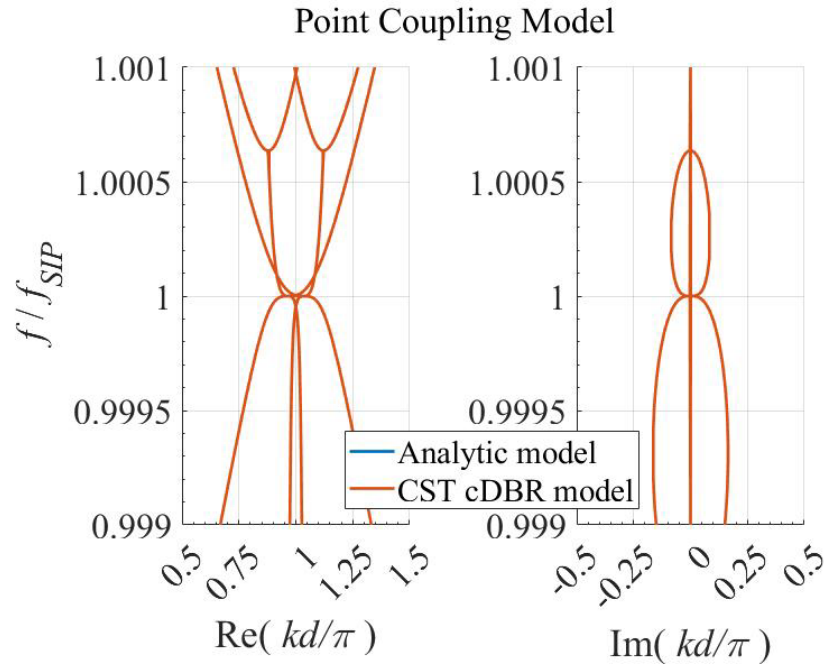
Figure 9. Point coupling model complex dispersion diagram of the infinite length unit cell structure using the analytic (lossless) and CST cDBR (lossy) models.

The dispersion diagram for the point coupling model with $\kappa = 0.273$, $L = 11.17\,\mu\text{m}$, $L' = 4.468\,\mu\text{m}$, $H = 1.737\,\mu\text{m}$ is shown in [Fig. 9](#) for the analytic (lossless) model and for the CST cDBR (lossy) model where $f_{SIP} = 193\,\text{THz}$. As expected, the two models are in very close agreement and only deviate close to the SIP as shown in [Fig. 10](#) where we zoom in on the SIP. We additionally show the evanescent and propagating branches of

the dispersion diagram in Fig. 11 for the analytic model where, for $\mathrm{Re}(kd/\pi)<1$, the SIP experiences a negative slope in the real part of the wavenumber. Above one the slope of the real wavenumber dispersion eigenmode is positive.
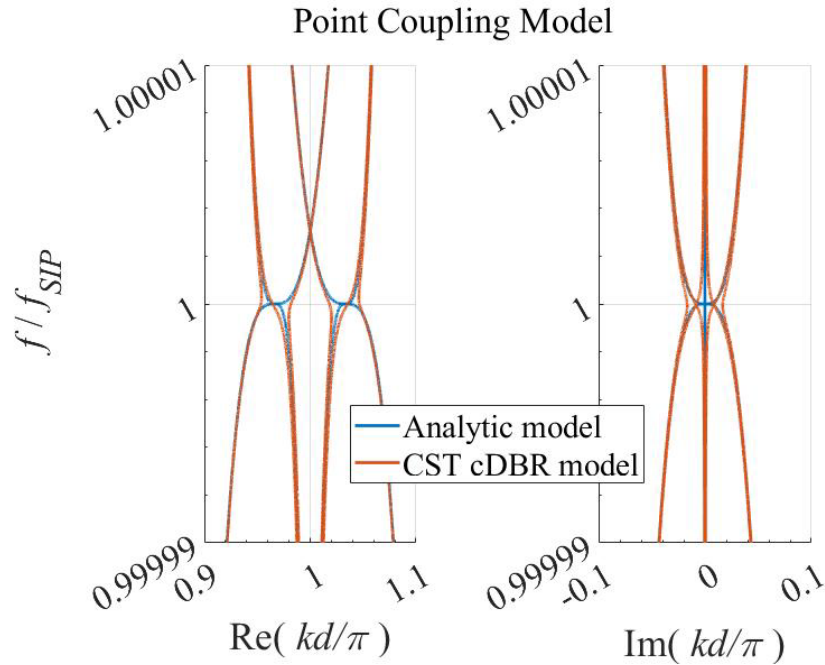
Figure 10. Point coupling model zoomed in complex dispersion diagram illustrating the differences between the two models at frequencies very close to the SIP frequency.

An additional useful view of the dispersion diagram is shown in Fig. 12 where the six eigenvalues are plotted with the imaginary component of their wavenumber versus the real part of their wavenumber. It is clear that three eigenmodes share the same real and imaginary wavenumber at the SIP and are offset 60° to each other directly before and after the SIP. Not only is this figure useful in visualizing the coalescence of the SIP, we can also plot the degree to which the unit cell transfer matrix solves the characteristic equation shown in Fig. 13. The depth of this contour plot represents how close the determinant for a given eigenvector is to zero on a logarithmic scale.

Point Coupling Model
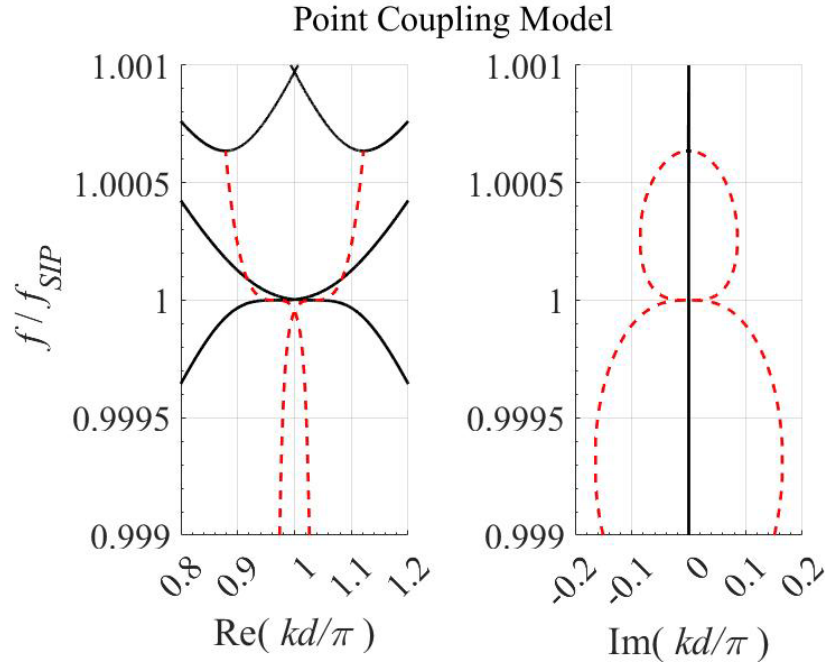
Figure 11. Dispersion diagram of the point coupling analytic model with the evanescent modes shown in red and propagating modes shown in black.
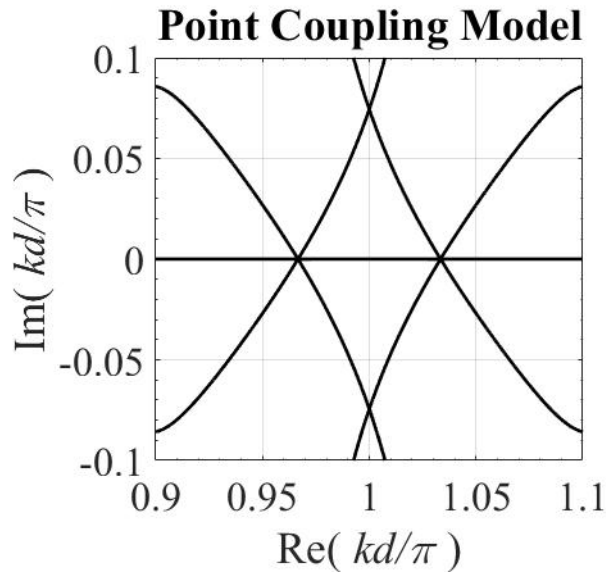
Figure 12. Imaginary versus real wavenumber of the dispersion diagram for the point coupling analytic model.
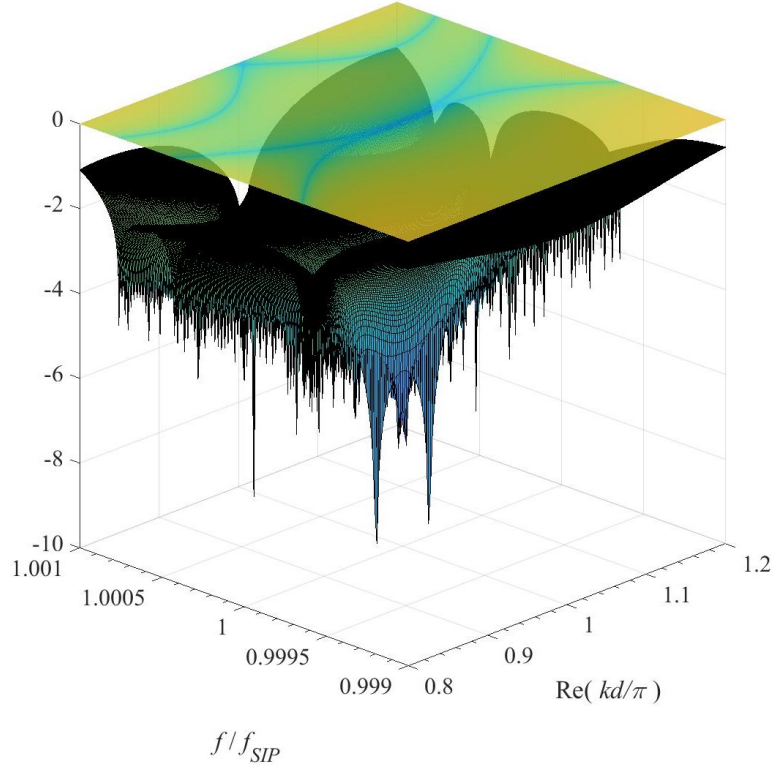
Figure 13. Contour of the propagating branches of the dispersion diagram for the point coupling analytic model.

We also notice that this particular SIP is close to the Brillouin Zone center with a normalized separation of less than 0.05 on each side of one. For the infinite length structure, there is no current consensus on the effect the closeness has on the quality of the SIP. However, for finite length models, interactions in the OWG because of the SIP closeness may cause a deterioration of the transfer function amplitude near the SIP resonance frequency. From iterative searching over the four parameter space, and even when modifying the cDBR design, efforts to move the SIP away from the Brillouin Zone center were unsuccessful. While the particular reason for this limit is unknown, we hypothesize the geometry may restrict movement of the SIP location to a range.

We now turn our discussion to the distributed coupling model instead of the point coupling model. As stated, the two primary differences in the point vs. distributed model are that the transfer matrix for the coupler uses the even/odd mode formulation and the full length of the cDBR is

considered. The same analysis for the characteristic equation and eigenvalues is performed for this model but with a different unit cell transfer matrix. In the distributed coupling model, we can construct the unit cell transfer matrix using four subblocks instead of five.

Similar to the point coupling model, the first and third subblock incorporate the cDBR and coupler. The first subblock has the cDBR relating the upper OWG field amplitudes and the distributed coupler relating the lower two OWG field amplitudes. In the third subblock, the roles are reversed. Also like the point coupling model, the second and fourth subblocks incorporate purely phase delay elements. Therefore, the subblock matrices describing these sections only have diagonal terms.

We note here two aspects of the distributed coupling model which are improvements over the point coupling model and two aspects of the distributed coupling model which do not accurately reflect the OWG behavior. As the cDBR clearly has an associated length, and coupling cannot occur at a singular location, incorporating the length of the cDBR and the length of the coupled waveguides are immediate improvements over un-realistic yet useful first order point like models. The arc length and radius of the middle OWG curved section is directly influenced by the cDBR length and the length of the coupler, so adding complexity to the model allows for a better approximation of the actual OWG modes.

A somewhat significant yet expected imperfection of the distributed coupling model involves including the coupling from the middle OWG curved section. As the middle waveguide arcs start curving, they experience a gradually decreasing coupling between the top and bottom waveguides as it approaches the center of the geometric height. This small but present coupling depends on the quickness the middle waveguide deviates from the straight top and bottom waveguides. The quicker the middle waveguide turns, the less coupling is added. Because the subblocks modeling

the curved section are only represented as phase delays, this additional coupling is not modeled or included in the unit cell transfer matrix. The quickness with which the middle waveguide deviates from the straight waveguides is proportional to the radius of curvature of the arcs. Therein lies the second imperfection in this distributed model: accounting for bending losses. As discussed previously, the smaller the radius of curvature, the more losses in the bend. The phase delay elements do not account for any amplitude decrease proportional to the radius of curvature. The two points discussed in this paragraph are left for further studies and research.

Now that we have described the distributed coupling model and its construction, we present similar diagrams to that of the point coupling model. Naturally, as seen from Fig. 1(a), we use different geometric parameters to describe the unit cell optimized for the SIP. These parameters are $L = 1.333$ μm, $L_c = 2.230$ μm, $H = 1.781$ μm and correspond to a unit cell period of $d = 11.895$ μm. Compared to the point coupling model, we have tried to minimize the unit cell length to decrease the physical footprint of the device and have achieved a reduction in approximately one third of the unit cell period. We also pushed the next closest RBE away from the SIP by approximately 250 GHz compared to the point coupling model which has a separation of approximately 130 GHz.

Figures 14 through 18 show the following: the dispersion relation of the unit cell for the distributed model; a zoomed in view highlighting the slight differences in the analytic and CST cDBR models; the propagating and evanescent modes; the real vs imaginary wavenumber; and a contour of the dispersion.
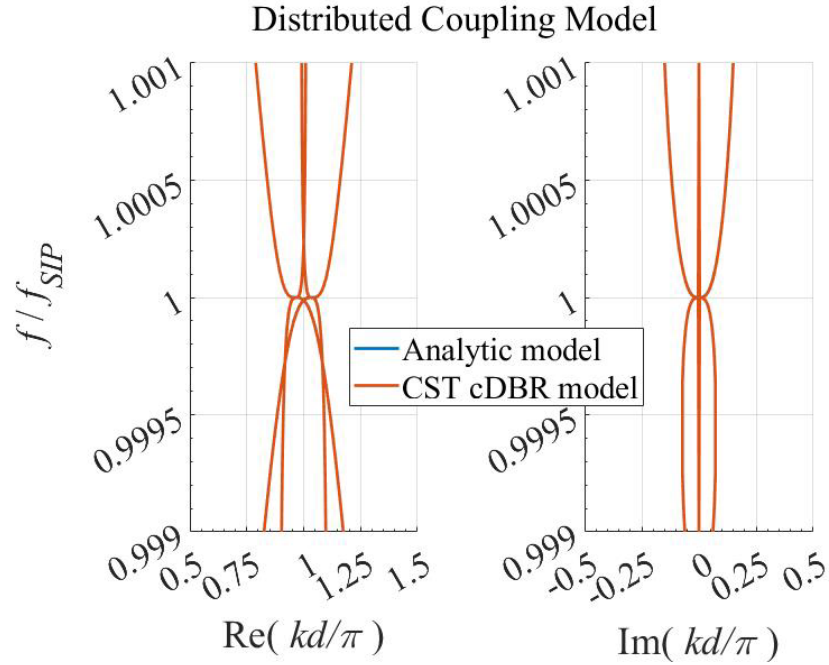
Figure 14. Distributed coupling model complex dispersion diagram of the infinite length unit cell structure using the analytic (lossless) and CST cDBR (lossy) models.
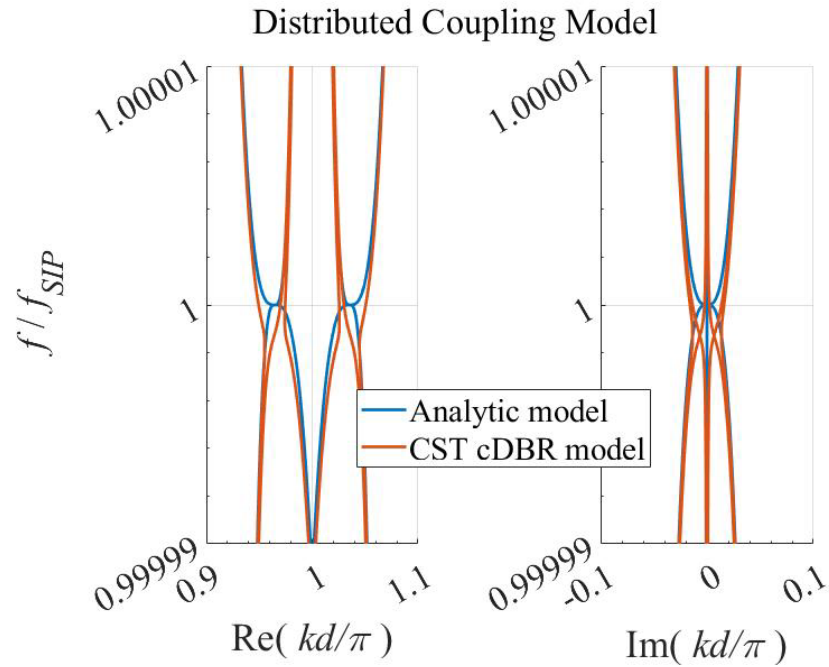
Figure 15. Distributed coupling model zoomed in complex dispersion diagram illustrating the differences between the two models at frequencies very close to the SIP frequency.
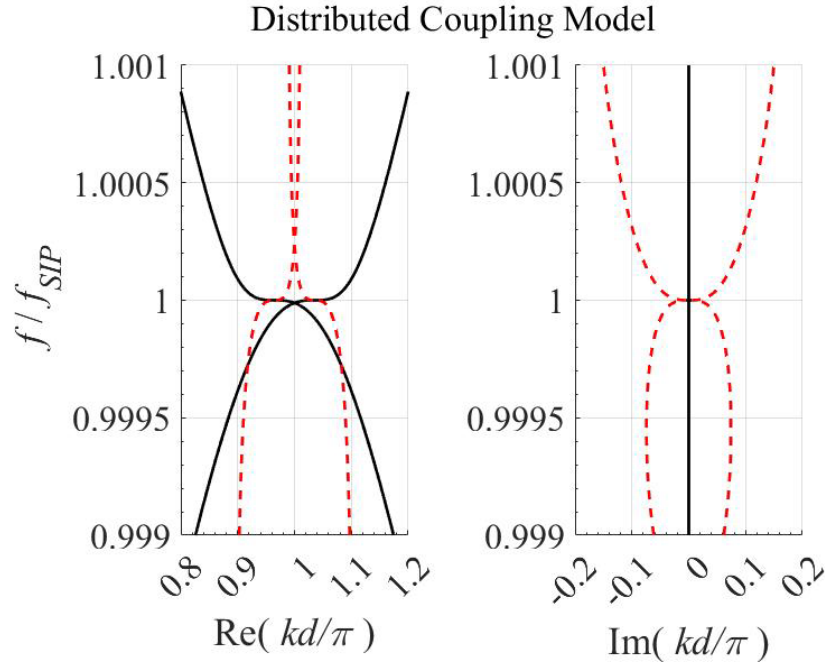
Figure 16. Dispersion diagram of the distributed coupling analytic model with the evanescent modes shown in red and propagating modes shown in black.
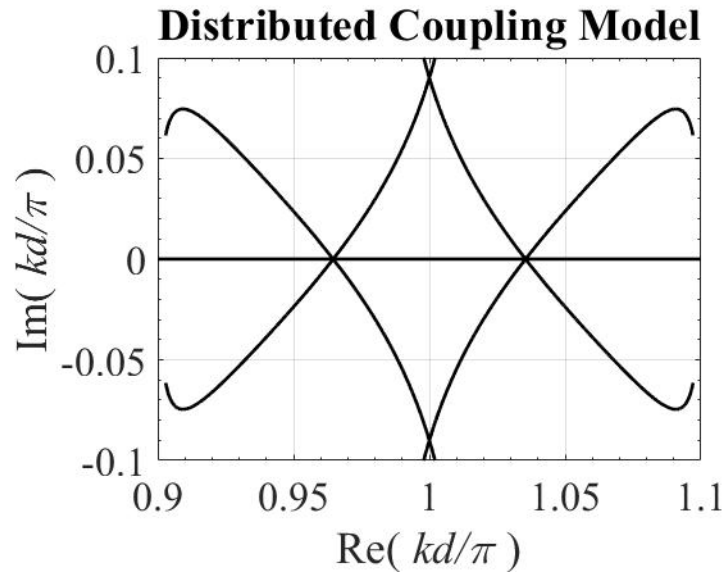
Figure 17. Imaginary versus real wavenumber of the dispersion diagram for the distributed coupling analytic model.
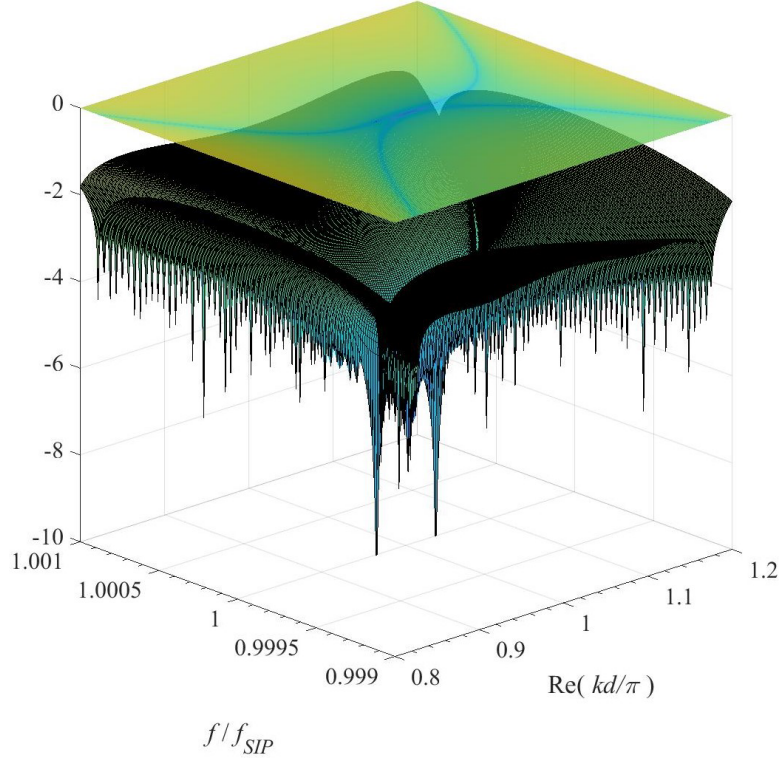
Figure 18. Contour of the propagating branches of the dispersion diagram for the distributed coupling analytic model.

In the distributed model, we have also tried to move the SIP away from the BZ center. After extensive searching of the parameter space, we were unable to characterize a SIP with more than ~0.04 normalized wavenumber spacing away from the BZ center.

In the vicinity near the SIP, the dispersion is characterized by ω_{SIP} and k_{SIP}, the angular frequency at which the three modes coalesce and the wavenumber at the SIP, respectively. Around f_{SIP}, the dispersion is well approximated by

$$\omega - \omega_{SIP} \approx \eta(k - k_{SIP})^3 \tag{2.5.2}$$

where η is a constant describing the flatness of the SIP.

As a final validation of the accuracy and drawbacks of the distributed coupling model, we have simulated the unit cell in CST. The simulation uses over 1.6 million tetrahedral mesh cells and a scattering parameter tolerance on the order of 10^{-4}. We highlight a few key elements of Fig. 19,

particularly the RBE seen in both the real and imaginary normalized wavenumber plots and the deviation from zero in the imaginary plot. The analytic distributed coupling model and the full CST simulation both exhibit a split in the real part of the wavenumber around 0.9985 and 0.998, respectively. The imaginary part of the wavenumber shows the same split. In the lossless analytic model, we see the imaginary part of the dispersion perfectly equal zero for some branches. In the full CST model, we see a slight deviation from zero for the same branches. This deviation is interpreted as losses resulting from the cDBR, the curved sections, and more.
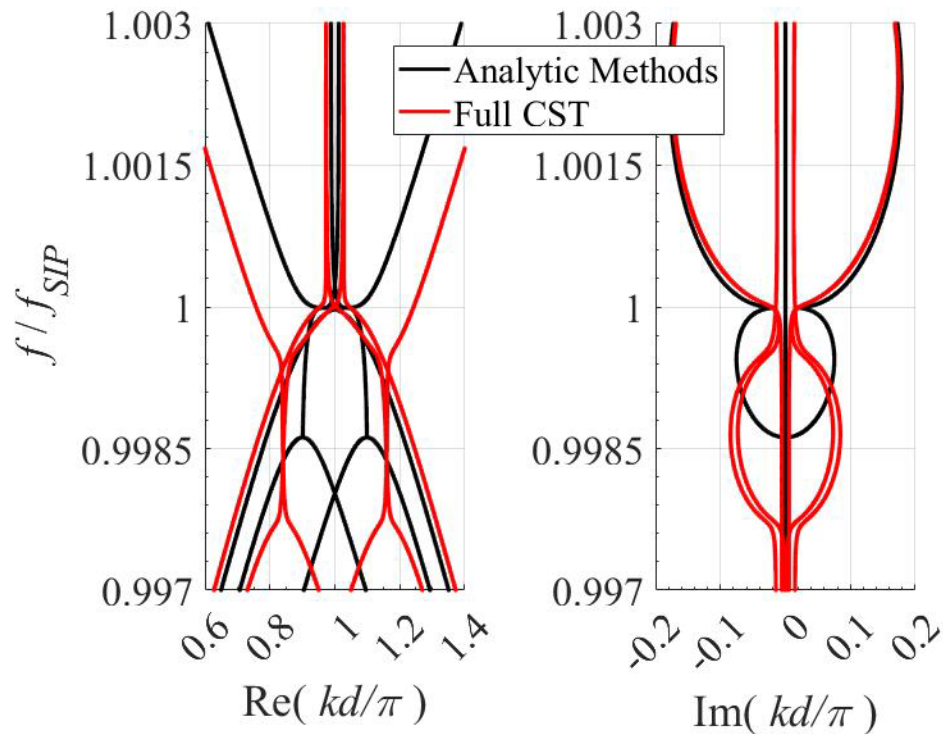
Figure 19. Comparison of the distributed coupling model to a full wave CST simulation of the same structure.

2.6 Validation of Third Order Exceptional Point

We can consider the closeness, or coalescence, of any given two eigenvector by the magnitude of the sine of angle between the eigenvectors. If two eigenvectors have the same magnitude and

36

direction, the magnitude of the sine of the angle between them is zero. Extending this idea to three eigenvectors, we simply take the algebraic average of the sine magnitude between the three positive eigenvectors. To calculate the sine between two vectors, we use the definition of the inner product normalized by the product of the vector's norms. Put more concisely, the coalescence parameter, which measures the extent to which three eigenvectors have degenerate eigenmodes, is given by

$$C = \frac{1}{3} \sum_{\substack{m=1,n=2 \\ n>m}}^{3} |\sin(\theta_{mn})|, \quad \cos(\theta_{mn}) = \frac{|\langle \Psi_m, \Psi_n \rangle|}{\|\Psi_m\| \ \|\Psi_n\|} \qquad (2.6.1)$$

where θ_{mn} is the angle between the two six-dimensional normalized complex state vectors [1], [2]. The inner product is defined as $\langle \Psi_m, \Psi_n \rangle = \Psi_m^{\dagger} \Psi_n$ with the dagger symbol † representing the complex conjugate transpose operation, or the Hermitian operation. $\|\Psi_m\|$ and $\|\Psi_n\|$ denote the norms of the two vectors, and with our six-port system, Ψ_1, Ψ_2, and Ψ_3 represent the three eigenvectors associated with the three positive wavenumbers in the dispersion diagram.

The coalescence parameter C is always positive and less than one, with zero representing perfect coalescence. At perfect coalescence, the system experiences the SIP. However, in any model and notably in practice, perfect coalescence is impossible and instead we say the system operates in the SIP regime or near the SIP. This impossibility is due to numerical errors where we can go arbitrarily close to the SIP, or due to losses either in fabrication, scattering losses, and more. The coalescence parameter for the analytic and CST cDBR models are shown in Fig. 20 for the point coupling and distributed coupling variations.

By minimizing the coalescence parameter through changes in the unit cell transfer matrix parameters, we can design a structure which operates in the SIP regime. The dispersion diagrams shown in the previous section were the result of such optimization in system parameters. It should

be noted, however, the reflection coefficient magnitude and angle are based on the CST cDBR design and were not directly included in the optimization. Once the main cDBR was designed, the scattering parameters were used as-is. This still provides great flexibility in designing the structure while reducing time and uncertainty associated with multiple iterative CST simulations.

In the analytic models, the threshold we set for the coalescence parameter to be considered a SIP was 10^{-4}, which again can be set arbitrarily close to zero. Replacing the lossless reflection transfer matrix with the lossy cDBR transfer matrix, we still see a coalescence parameter around 10^{-1}. While this value is orders of magnitude larger than for the lossless model, based on the dispersion diagram and the contour of the dispersion diagram, we can still say the structure is operating in the SIP regime.

Point Coupling Model

(a)

Distributed Coupling Model
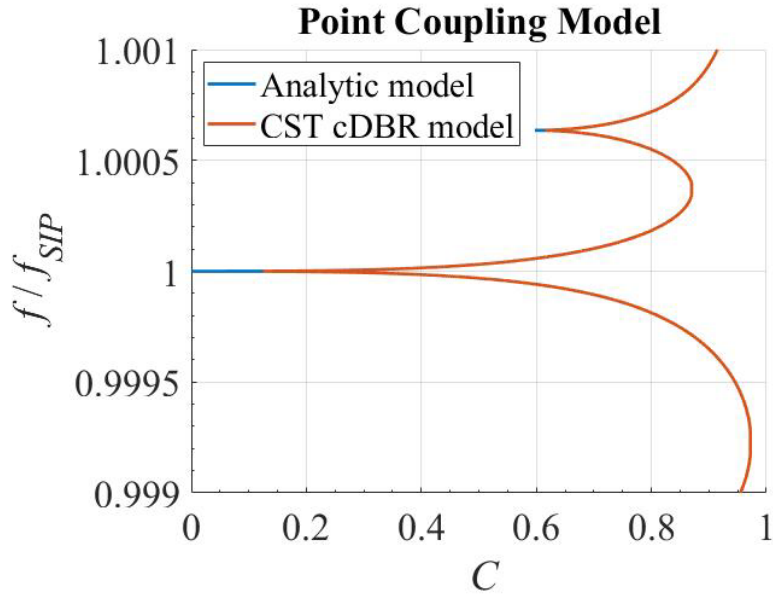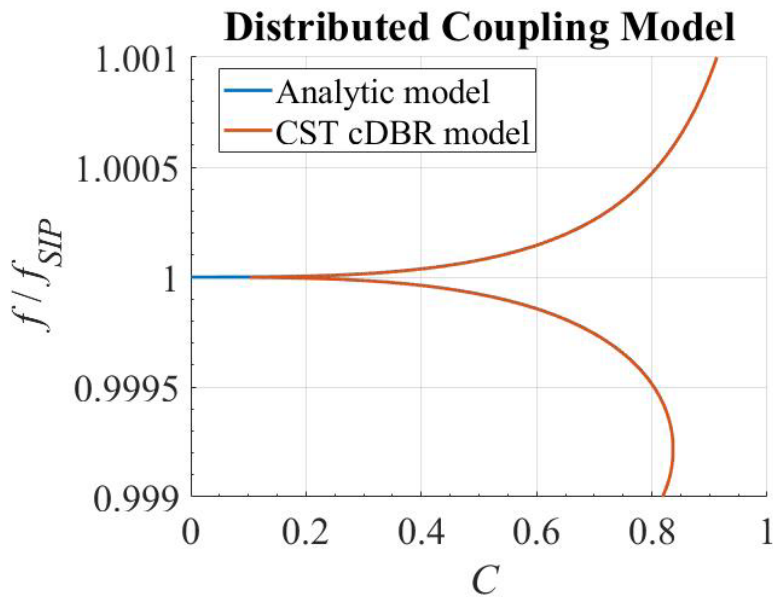
(b)

Figure 20. Coalescence parameter calculated for (a) the point coupling and (b) the distributed coupling models representing the amount of degeneracy in the eigenmodes. A zero value corresponds to perfect coalescence.

2.7 Summary

This section detailed the state vector used to describe the electric field propagation over a given distance and an alternate representation useful for multiple conversions. Equations were also given to transform transfer matrices representing the two state vectors. These details proved to be important when modeling the directional coupler based on commonly known field relationships.

The transfer matrices of each system subblock were also given in terms of the appropriate state vector and variables used to describe physical behavior. We detailed the design of a DBR and then a less lossy cDBR along with taking note of normalization impedances. We also detailed the modeling of coupled waveguides using even and odd modes along with the conversion to forward and backward fields. The construction of the middle OWG curved sections was presented with equations to calculate the radius of curvature for the arcs. Using all of the subblocks, we described how the full unit cell transfer matrix is built for the point coupling model and the distributed coupling model.

Finally, the dispersion relationship was discussed based on the infinite length structure and Floquet-Bloch theory. We described how we found the eigenmodes and highlighted key aspects of the dispersion diagram. The system appears to behave in the SIP regime based on modal structure and dispersion diagram behavior. Using the coalescence parameter, we further verified SIP behavior. The agreement between the lossless or analytic model and the lossy or cDBR model is also strikingly accurate due to the minimal losses in the cDBR model. This holds true for the point and disturbed coupling models. We can detect these losses both from a divergence from the $\mathrm{Im}(kd\,/\,\pi) = 0$ vertical line and from the increase of the coalescence parameter.

FINITE LENGTH ANALYSIS

3.1 Boundary Conditions

When performing a finite length analysis, we must set termination conditions on the six ports of the waveguide and determine which ports will be used as the input and output. For this structure, we terminate the bottom and middle waveguide with perfectly reflecting mirrors and consider the top waveguide terminated with matched waveguides on either end to prevent additional reflections. In practice, the middle and bottom waveguides may have broadband DBRs with very high reflectivity around 193 THz and the top waveguides may have impedance matching optics included. However, for simplicity and conciseness, these factors will not be discussed further here.

It is also possible for the input and output to be taken from any of the six ports unlike some other photonic structures such as a coupled resonator optical waveguide (CROW) or serpentine optical waveguide (SOW) [1], [19], [57]. While we have performed analysis on various input/output arrangements, using the top waveguide as the input and output appears to be sufficient for finite length models.

For the sake of reducing repeated analysis, we will only discuss the distributed coupling model in the following sections. As the point coupling model and distributed coupling model have similarities in accuracy, the distributed coupling model is a more accurate model and thus the primary focus for finite length analysis.

Taking the unit cell as in Fig. 1(b), we modify the repeating structure so the input and output waveguides are not terminated by the cDBR and coupled waveguides. For the additional leftmost segment, we remove the cDBR and the distributed coupler and add a length to the upper waveguide to match with the lower two waveguides. Similarly, for the additional rightmost unit, we remove

41

the coupled section and extend the topmost waveguide to match the lower two waveguides. The additional segments are denoted and described as the auxiliary transfer matrix $\underline{\mathbf{T}}_A$ and the auxiliary transfer matrix $\underline{\mathbf{T}}_B$. Fig. 21 shows the geometry for the two auxiliary segments.

(a)

(b)
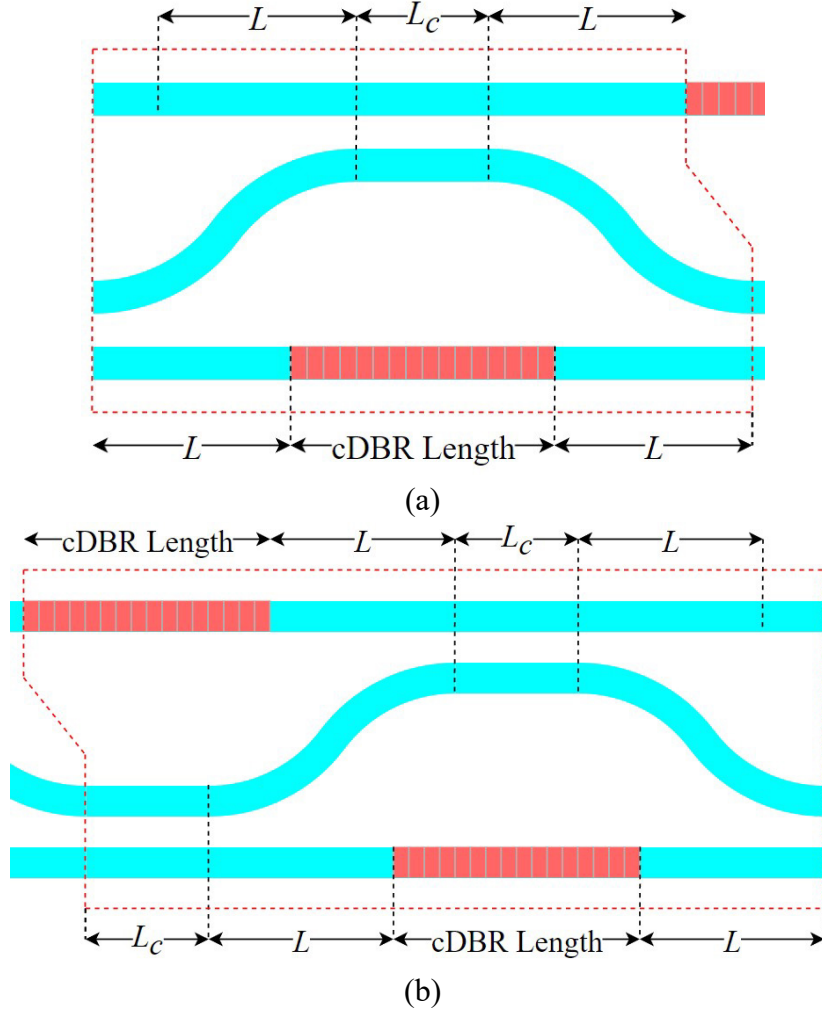
Figure 21. Auxiliary finite length segments for (a) the start of the unit cell and (b) the end of the unit cell.

3.2 Transfer and Reflection Functions

From the previous section, we take both the input and output from the top waveguide. If we have N unit cells of length d beginning at $z = 0$, we can write the transfer function at the output as

$$T_f = \frac{E_1^+(Nd+d')}{E_1^-(0)} \tag{3.2.1}$$

where d' is the added length from the auxiliary geometries.

Similarly, we can write the reflection function as

$$R_f = \frac{E_1^-(0)}{E_1^+(0)} \tag{3.2.2}$$
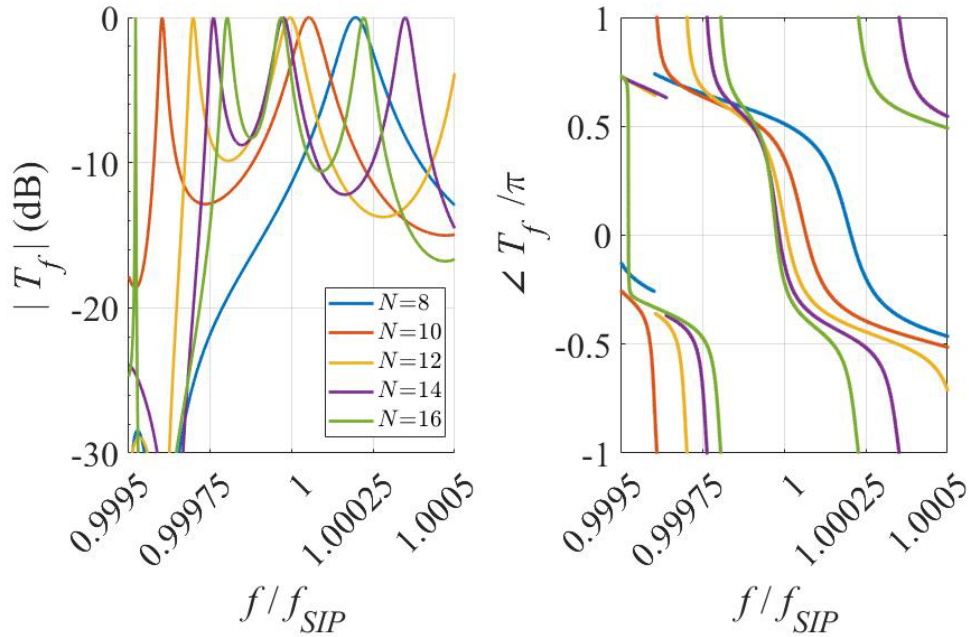
Figure 22. Magnitude in dB and phase normalized to π of the transfer function for a given number of unit cells *N*.

If we normalize the electric field at the input to one, the transfer function and reflection function are simplified in further calculations. To calculate these functions, we calculate the transfer matrix for one unit cell and cascade the matrix *N* times to find the state vector at the output as described by

$$\Psi(z = Nd+d') = \underline{\mathbf{T}}_B \underline{\mathbf{T}}_U^N \underline{\mathbf{T}}_A \Psi(z=0) \tag{3.2.3}$$

where $\underline{\mathbf{T}}_A$ and $\underline{\mathbf{T}}_B$ are described in Fig. 21.

43

Fig. 22 and Fig. 23 show the transfer and reflection function magnitude and phase for a few different numbers of unit cells. Sharp jumps in the transfer function phase plot are partially due to wrapping around the unit circle every 2π. The phase plots are normalized to π for better readability. As we increase the number of unit cells to infinity in the analytic model, we expect unity magnitude at the SIP frequency. With more unit cells, our model conforms more to Floquet-Bloch theory of periodic structures. There is, however, a tradeoff in the number of unit cells, complexity, and size of the structure, especially when considering a real, lossy, system. As the number of unit cells increase, the dimensions of the system may become too large and losses may compound to provide no clear benefit to operating in the SIP regime. Conversely, not enough unit cells and the structure cannot realize any characteristics of SIP behavior as the waves in the structure have not been able to propagate and interfere enough. As a result, we consider N between approximately six and twenty.

From the transfer and reflection functions, we can clearly see a trend in the peaks and valleys close to the SIP as the number of unit cells increase. With eight unit cells (the blue curve), the transfer function peak is about 0.0002 f/f away from the SIP, or approximately 37 GHz in absolute frequency units. As we approach 16 unit cells (the green curve), the peak is spaced only 6 GHz away from the ideal Floquet-Bloch analysis. We also see a similar trend at frequencies lower than the SIP frequency where the peaks of the transfer function seem to converge with more unit cells. Without further analysis, either peak could correspond to the SIP resonance predicted in the infinite unit cell description. We will see shortly how the group delay may shed light on the trends seen in the transfer and reflection function plots.
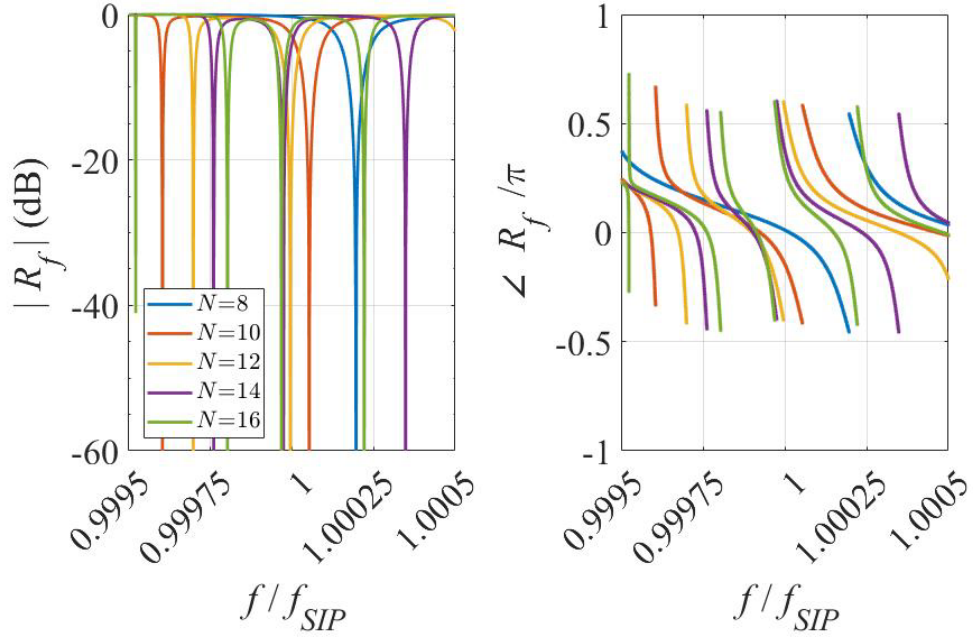
Figure 23. Magnitude in dB and phase normalized to π of the reflection function for a given number of unit cells *N*.

3.3 Quality Factor and Group Delay

Two important figures of merit in a finite length cavity are the quality factor and group delay. We use the standard definition of the group delay as

$$\tau_g = -\frac{\partial \angle T_f(\omega)}{\partial \omega} \tag{3.3.1}$$

and we use the definition of the quality factor based on the group delay as

$$Q = \frac{\omega_{SIP,res}\tau_g}{2} \approx \frac{\omega_{SIP}\tau_g}{2} \tag{3.3.2}$$

where we approximate the SIP resonance frequency as the ideal SIP frequency for frequencies of interest.
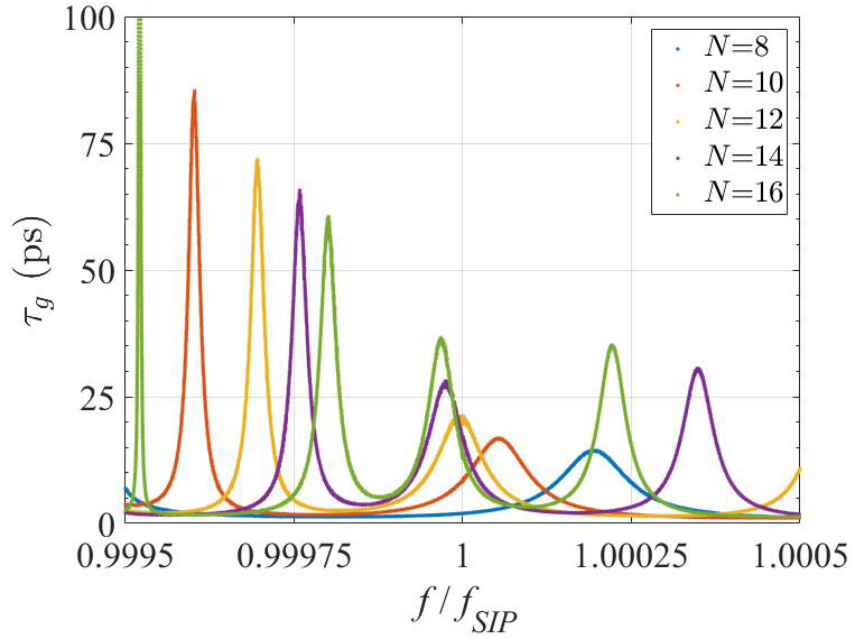
Figure 24. Group delay of the finite length structure for a given number of unit cells.

Before detailing the group delay and quality factor plots, it is helpful to describe the SIP resonance frequency $f_{SIP,res}$ as the frequency closest to the SIP frequency f_{SIP} where the reflection function is minimal. There may also be consideration before choosing the closest valley to the SIP frequency as the SIP resonance frequency. As the number of unit cells increase, we may notice a trend in the transfer and reflection functions as described in the prior section. Thus, if there is a valley in the reflection function for a given number of unit cells which is closer to the SIP frequency yet does not experience the described trend, the closer valley may not be the SIP resonance frequency in the finite length structure. We see this clearly in Fig. 24 where the group delay is experiencing a seemingly linear decrease as the number of unit cells increase for normalized frequencies around 0.99975. We compare this decreasing trend to frequencies very close to the SIP frequency which are experiencing an increasing trend. Although only a limited

number of unit cells are displayed in the figure, we verify that as the number of unit cells continues to increase the increasing trend closest to the SIP frequency dominates.
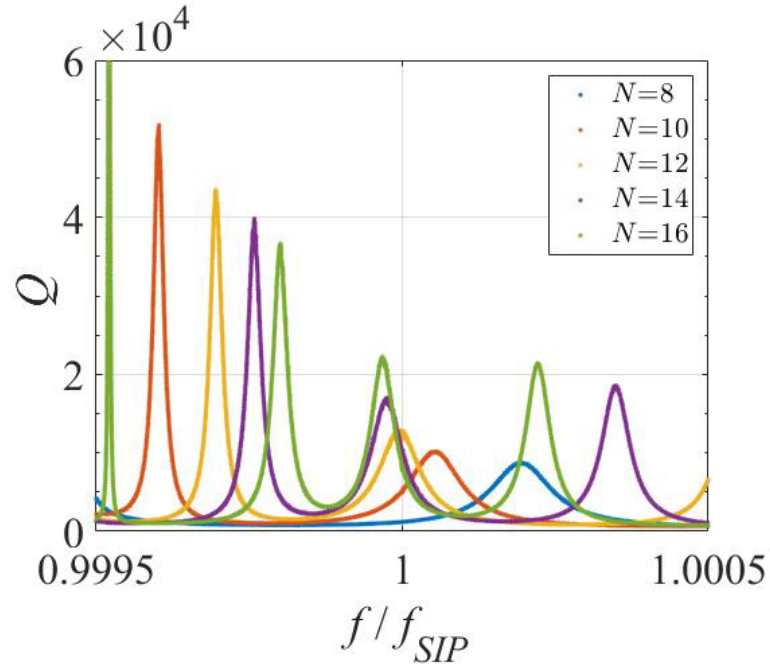
Figure 25. Quality factor of the finite length structure for a given number of unit cells.

A key characteristic of the SIP is zero group velocity, or a frozen mode at the SIP. Equivalently, the group delay at the SIP is infinite. Due to the structure being finite, we only see peaks in the group delay in the SIP regime.

We also show trends in the group delay in Fig. 26 at the SIP resonance frequency. As the number of unit cells increase, we notice a cubic relationship between the maximum of the group delay and number of unit cells, expressed at $\tau_{g,max} \propto aN^3 + b$ where a and b are fitting constants. Based on Fig. 26, $a = 6.54\,\text{fs}$ and $b = 24.36\,\text{ps}$. We can also numerically describe the improvement in group delay over a straight waveguide of equal length. We calculate the delay in a straight waveguide as Nd/v_{ph} where $v_{ph} \approx 1.275 \times 10^8\,\text{m/s}$ was calculated from CST Studio Suite and d includes the two auxiliary cells. For an equivalent $N = 30$ non-SIP structure (total

length $\approx$ 400 μm) the group delay is 3.13 ps compared a group delay at the SIP resonance of 190 ps. This gives an increase in group delay over 60 times that of the non-SIP structure.
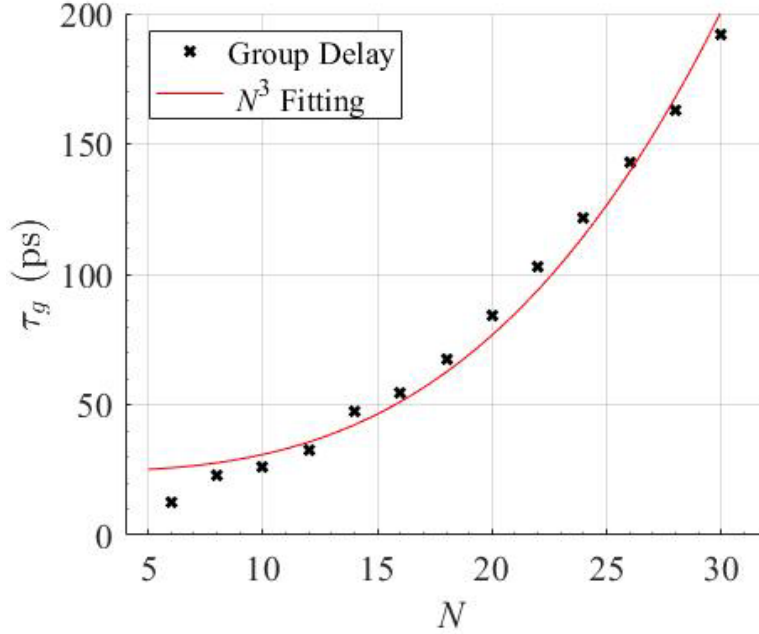
Figure 26. Group delay at the SIP resonance frequency for a given number of unit cells *N*. The fitting curve is described by $aN^3 + b$ where a = 6.54 fs and b = 24.36 ps.

3.4 Summary

Analyzing the finite length structure involves careful consideration of boundary conditions and the termination of each waveguide port. Approximating ideal reflections to terminate the middle and bottom waveguide ports and connecting equal impedance waveguides to the input and output ports, we calculated important aspects of the finite length structure with auxiliary blocks added to the unit cell. The transfer and reflection functions were calculated using the unit cell transfer matrix cascaded *N* times for the number of unit cells. As $N \to \infty$, the structure operates more like ideal Floquet-Bloch theory when not accounting for losses.

The group delay and quality factor were also presented with some discussion on the differences between the SIP frequency and the SIP resonance frequency. The group delay and thus the quality factor experienced third order scaling based on the number of unit cell included. This scaling is consistent with other SIP geometries and further verifies operation in the SIP regime.

CONCLUSION AND FUTURE WORK

The field of exceptional points of degeneracy is growing rapidly as more systems are designed, analyzed, and fabricated. New applications of this theory are discovered regularly and may significantly affect a variety of fields from quantum computing to biomedicine. This section gives an overview of some applications of the third order degeneracy or stationary inflection point along with next steps in SIP devices. In this thesis, an optical waveguide design has been presented that operates in the SIP regime with both lossless and lossy models along with considering point coupling/reflections and distributed coupling/reflections. The finite length structure based on the waveguide unit cell exhibits expected yet interesting power scaling of the group delay and quality factor.

We have optimized the design using the coalescence parameter as the primary figure of merit and a cDBR with an order of magnitude less loss than its DBR counterpart. Three geometric parameters are used to describe the unit cell structure along with the directional coupler coupling coefficient and cDBR scattering matrix. This SIP, while close to the Brillouin Zone center, is isolated from other EPDs by a relatively large bandwidth of approximately 250 GHz.

SIP structures may be useful in a handful of devices, including optical delay lines, very sensitive sensors, lasers, and more. With an exponential increase in the group delay of an incident signal, all-optical routers and switches are more feasible because of the increased time for coherent light storage. EPDs are also generally sensitive to perturbations and may be tuned to be either more or less robust to parameter variations. This behavior can be used in sensing devices to detect changes much finer than non-SIP counterparts.

The last application to discuss, lasers, is also the topic of significant future work. As the dispersion diagram does not have a stop-band and remains monotonically increasing or decreasing

depending on the wavenumber for propagating eigenmodes, lasers operating in the SIP regime show great promise. More work is needed to determine conditions for lasing and how to fabricate waveguides in silicon which exhibit the discussed properties.

REFERENCES

[1] M. Y. Nada, M. A. K. Othman, and F. Capolino, "Theory of coupled resonator optical waveguides exhibiting high-order exceptional points of degeneracy," *Phys. Rev. B*, vol. 96, no. 18, p. 184304, Nov. 2017, doi: 10.1103/PhysRevB.96.184304.

[2] M. Y. Nada, T. Mealy, and F. Capolino, "Frozen Mode in Three-Way Periodic Microstrip Coupled Waveguide," *IEEE Microw. Wirel. Compon. Lett.*, vol. 31, no. 3, pp. 229–232, Mar. 2021, doi: 10.1109/LMWC.2020.3042205.

[3] Ş. K. Özdemir, S. Rotter, F. Nori, and L. Yang, "Parity–time symmetry and exceptional points in photonics," *Nat. Mater.*, vol. 18, no. 8, pp. 783–798, Aug. 2019, doi: 10.1038/s41563-019-0304-9.

[4] A. Figotin and I. Vitebskiy, "Oblique frozen modes in periodic layered media," *Phys. Rev. E*, vol. 68, no. 3, p. 036609, Sep. 2003, doi: 10.1103/PhysRevE.68.036609.

[5] T. Kato, *Perturbation theory for linear operators*, 2. ed. Berlin Heidelberg: Springer, 1976. doi: 10.1007/978-3-642-66282-9.

[6] W. D. Heiss, "Exceptional points of non-Hermitian operators," *J. Phys. Math. Gen.*, vol. 37, no. 6, pp. 2455–2464, Feb. 2004, doi: 10.1088/0305-4470/37/6/034.

[7] W. D. Heiss, "The physics of exceptional points," *J. Phys. Math. Theor.*, vol. 45, no. 44, p. 444016, Nov. 2012, doi: 10.1088/1751-8113/45/44/444016.

[8] C. M. Bender and S. Boettcher, "Real Spectra in Non-Hermitian Hamiltonians Having PT Symmetry," *Phys. Rev. Lett.*, vol. 80, no. 24, pp. 5243–5246, Jun. 1998, doi: 10.1103/PhysRevLett.80.5243.

[9] G. W. Hanson, A. B. Yakovlev, M. A. K. Othman, and F. Capolino, "Exceptional Points of Degeneracy and Branch Points for Coupled Transmission Lines—Linear-Algebra and Bifurcation Theory Perspectives," *IEEE Trans. Antennas Propag.*, vol. 67, no. 2, pp. 1025–1034, Feb. 2019, doi: 10.1109/TAP.2018.2879761.

[10] T. Mealy, A. F. Abdelshafy, and F. Capolino, "The Degeneracy of the Dominant Mode in Rectangular Waveguide," in *2019 United States National Committee of URSI National Radio Science Meeting (USNC-URSI NRSM)*, Boulder, CO, USA, Jan. 2019, pp. 1–2. doi: 10.23919/USNC-URSI-NRSM.2019.8712950.

[11] W. Chen, Ş. Kaya Özdemir, G. Zhao, J. Wiersig, and L. Yang, "Exceptional points enhance sensing in an optical microcavity," *Nature*, vol. 548, no. 7666, pp. 192–196, Aug. 2017, doi: 10.1038/nature23281.

[12] J. Wiersig, "Enhancing the Sensitivity of Frequency and Energy Splitting Detection by Using Exceptional Points: Application to Microcavity Sensors for Single-Particle Detection," *Phys. Rev. Lett.*, vol. 112, no. 20, p. 203901, May 2014, doi: 10.1103/PhysRevLett.112.203901.

[13] A. Figotin and I. Vitebskiy, "Frozen light in photonic crystals with degenerate band edge," *Phys. Rev. E*, vol. 74, no. 6, p. 066613, Dec. 2006, doi: 10.1103/PhysRevE.74.066613.

[14] M. Veysi, M. A. K. Othman, A. Figotin, and F. Capolino, "Degenerate band edge laser," *Phys. Rev. B*, vol. 97, no. 19, p. 195107, May 2018, doi: 10.1103/PhysRevB.97.195107.

[15] A. F. Abdelshafy, D. Oshmarin, M. A. K. Othman, M. M. Green, and F. Capolino, "Distributed Degenerate Band Edge Oscillator," *IEEE Trans. Antennas Propag.*, vol. 69, no. 3, pp. 1821–1824, Mar. 2021, doi: 10.1109/TAP.2020.3018539.

[16]   J. L. Volakis and K. Sertel, "Narrowband and Wideband Metamaterial Antennas Based on Degenerate Band Edge and Magnetic Photonic Crystals," *Proc. IEEE*, vol. 99, no. 10, pp. 1732–1745, Oct. 2011, doi: 10.1109/JPROC.2011.2115230.

[17]   M. A. K. Othman, F. Yazdi, A. Figotin, and F. Capolino, "Giant gain enhancement in photonic crystals with a degenerate band edge," *Phys. Rev. B*, vol. 93, no. 2, p. 024301, Jan. 2016, doi: 10.1103/PhysRevB.93.024301.

[18]   A. Figotin and I. Vitebskiy, "Gigantic transmission band-edge resonance in periodic stacks of anisotropic layers," *Phys. Rev. E*, vol. 72, no. 3, p. 036619, Sep. 2005, doi: 10.1103/PhysRevE.72.036619.

[19]   M. Y. Nada, M. A. K. Othman, O. Boyraz, and F. Capolino, "Giant Resonance and Anomalous Quality Factor Scaling in Degenerate Band Edge Coupled Resonator Optical Waveguides," *J. Light. Technol.*, vol. 36, no. 14, pp. 3030–3039, Jul. 2018, doi: 10.1109/JLT.2018.2822600.

[20]   W. D. Heiss, M. Müller, and I. Rotter, "Collectivity, phase transitions, and exceptional points in open quantum systems," *Phys. Rev. E*, vol. 58, no. 3, pp. 2894–2901, Sep. 1998, doi: 10.1103/PhysRevE.58.2894.

[21]   R. El-Ganainy, K. G. Makris, D. N. Christodoulides, and Z. H. Musslimani, "Theory of coupled optical PT-symmetric structures," *Opt. Lett.*, vol. 32, no. 17, p. 2632, Sep. 2007, doi: 10.1364/OL.32.002632.

[22]   S. Klaiman, U. Günther, and N. Moiseyev, "Visualization of Branch Points in PT -Symmetric Waveguides," *Phys. Rev. Lett.*, vol. 101, no. 8, p. 080402, Aug. 2008, doi: 10.1103/PhysRevLett.101.080402.

[23]   C. E. Rüter, K. G. Makris, R. El-Ganainy, D. N. Christodoulides, M. Segev, and D. Kip, "Observation of parity–time symmetry in optics," *Nat. Phys.*, vol. 6, no. 3, pp. 192–195, Mar. 2010, doi: 10.1038/nphys1515.

[24]   S. Bittner *et al.*, "PT Symmetry and Spontaneous Symmetry Breaking in a Microwave Billiard," *Phys. Rev. Lett.*, vol. 108, no. 2, p. 024101, Jan. 2012, doi: 10.1103/PhysRevLett.108.024101.

[25]   A. Regensburger, C. Bersch, M.-A. Miri, G. Onishchukov, D. N. Christodoulides, and U. Peschel, "Parity–time synthetic photonic lattices," *Nature*, vol. 488, no. 7410, pp. 167–171, Aug. 2012, doi: 10.1038/nature11298.

[26]   G. Castaldi, S. Savoia, V. Galdi, A. Alù, and N. Engheta, "PT Metamaterials via Complex-Coordinate Transformation Optics," *Phys. Rev. Lett.*, vol. 110, no. 17, p. 173901, Apr. 2013, doi: 10.1103/PhysRevLett.110.173901.

[27]   A. Regensburger *et al.*, "Observation of Defect States in PT -Symmetric Optical Lattices," *Phys. Rev. Lett.*, vol. 110, no. 22, p. 223902, May 2013, doi: 10.1103/PhysRevLett.110.223902.

[28]   M. Wimmer, A. Regensburger, M.-A. Miri, C. Bersch, D. N. Christodoulides, and U. Peschel, "Observation of optical solitons in PT-symmetric lattices," *Nat. Commun.*, vol. 6, no. 1, p. 7782, Nov. 2015, doi: 10.1038/ncomms8782.

[29]   I. V. Barashenkov, L. Baker, and N. V. Alexeeva, "PT-symmetry breaking in a necklace of coupled optical waveguides," *Phys. Rev. A*, vol. 87, no. 3, p. 033819, Mar. 2013, doi: 10.1103/PhysRevA.87.033819.

[30]   J. K. S. Poon, J. Scheuer, Y. Xu, and A. Yariv, "Designing coupled-resonator optical waveguide delay lines," *J. Opt. Soc. Am. B*, vol. 21, no. 9, p. 1665, Sep. 2004, doi: 10.1364/JOSAB.21.001665.

[31] B. Paul, N. K. Nahar, and K. Sertel, "Frozen mode in coupled silicon ridge waveguides for optical true time delay applications," *J. Opt. Soc. Am. B*, vol. 38, no. 5, p. 1435, May 2021, doi: 10.1364/JOSAB.417281.

[32] K. J. Vahala, "Optical microcavities," *Nature*, vol. 424, no. 6950, pp. 839–846, Aug. 2003, doi: 10.1038/nature01939.

[33] H. Ramezani, T. Kottos, R. El-Ganainy, and D. N. Christodoulides, "Unidirectional nonlinear PT-symmetric optical structures," *Phys. Rev. A*, vol. 82, no. 4, p. 043803, Oct. 2010, doi: 10.1103/PhysRevA.82.043803.

[34] C.-L. Zou *et al.*, "Guiding light through optical bound states in the continuum for ultrahigh-Q microresonators," *Laser Photonics Rev.*, vol. 9, no. 1, pp. 114–119, Jan. 2015, doi: 10.1002/lpor.201400178.

[35] G. Mumcu, K. Sertel, and J. L. Volakis, "Printed coupled lines with lumped loads for realizing degenerate band edge and magnetic photonic crystal modes," in *2008 IEEE Antennas and Propagation Society International Symposium*, San Diego, CA, Jul. 2008, pp. 1–4. doi: 10.1109/APS.2008.4619592.

[36] H. Ramezani, S. Kalish, I. Vitebskiy, and T. Kottos, "Unidirectional Lasing Emerging from Frozen Light in Nonreciprocal Cavities," *Phys. Rev. Lett.*, vol. 112, no. 4, p. 043904, Jan. 2014, doi: 10.1103/PhysRevLett.112.043904.

[37] F. Yazdi, M. A. K. Othman, M. Veysi, F. Capolino, and A. Figotin, "Third order modal degeneracy in waveguids: Features and application in amplifiers," in *2017 USNC-URSI Radio Science Meeting (Joint with AP-S Symposium)*, San Diego, CA, USA, Jul. 2017, pp. 109–110. doi: 10.1109/USNC-URSI.2017.8074921.

[38] F. Yazdi, M. A. K. Othman, M. Veysi, A. Figotin, and F. Capolino, "A New Amplification Regime for Traveling Wave Tubes With Third-Order Modal Degeneracy," *IEEE Trans. Plasma Sci.*, vol. 46, no. 1, pp. 43–56, Jan. 2018, doi: 10.1109/TPS.2017.2781245.

[39] J. Schnabel, H. Cartarius, J. Main, G. Wunner, and W. D. Heiss, "PT-symmetric waveguide system with evidence of a third-order exceptional point," *Phys. Rev. A*, vol. 95, no. 5, p. 053868, May 2017, doi: 10.1103/PhysRevA.95.053868.

[40] J. K. S. Poon, J. Scheuer, Y. Xu, and A. Yariv, "Designing coupled-resonator optical waveguide delay lines," *J. Opt. Soc. Am. B*, vol. 21, no. 9, p. 1665, Sep. 2004, doi: 10.1364/JOSAB.21.001665.

[41] F. Xia, L. Sekaric, and Y. Vlasov, "Ultracompact optical buffers on a silicon chip," *Nat. Photonics*, vol. 1, no. 1, pp. 65–71, Jan. 2007, doi: 10.1038/nphoton.2006.42.

[42] S. L. McCall, A. F. J. Levi, R. E. Slusher, S. J. Pearton, and R. A. Logan, "Whispering-gallery mode microdisk lasers," *Appl. Phys. Lett.*, vol. 60, no. 3, pp. 289–291, Jan. 1992, doi: 10.1063/1.106688.

[43] T. Barwicz *et al.*, "Microring-resonator-based add-drop filters in SiN: fabrication and analysis," *Opt. Express*, vol. 12, no. 7, p. 1437, 2004, doi: 10.1364/OPEX.12.001437.

[44] A. A. Sukhorukov, C. J. Handmer, C. M. de Sterke, and M. J. Steel, "Slow light with flat or offset band edges in few-mode fiber with two gratings," *Opt. Express*, vol. 15, no. 26, p. 17954, 2007, doi: 10.1364/OE.15.017954.

[45] D. M. Pozar, *Microwave engineering*, 3rd ed. Hoboken, NJ: J. Wiley, 2005.

[46] G. Gonzalez, *Microwave transistor amplifiers: analysis and design*, 2nd ed. Upper Saddle River, N.J: Prentice Hall, 1997.

[47] L. B. Felsen and W. K. Kahn, "Transfer characteristics of 2N-port networks," in *Symposium on Millimeter Waves*, Brooklyn, New York, Mar. 1959, pp. 477–512.

[48]   M. A. K. Othman and F. Capolino, "Demonstration of a Degenerate Band Edge in Periodically-Loaded Circular Waveguides," *IEEE Microw. Wirel. Compon. Lett.*, vol. 25, no. 11, pp. 700–702, Nov. 2015, doi: 10.1109/LMWC.2015.2479845.

[49]   J. E. Heebner, Vincent Wong, A. Schweinsberg, R. W. Boyd, and D. J. Jackson, "Optical transmission characteristics of fiber ring resonators," *IEEE J. Quantum Electron.*, vol. 40, no. 6, pp. 726–730, Jun. 2004, doi: 10.1109/JQE.2004.828232.

[50]   R. März, *Integrated optics: design and modeling*. Boston: Artech House, 1995.

[51]   S. M. Mishkat-Ul-Masabih, A. A. Aragon, M. Monavarian, T. S. Luk, and D. F. Feezell, "Electrically injected nonpolar GaN-based VCSELs with lattice-matched nanoporous distributed Bragg reflector mirrors," *Appl. Phys. Express*, vol. 12, no. 3, p. 036504, Mar. 2019, doi: 10.7567/1882-0786/ab0576.

[52]   P. Modh, N. Eriksson, M. Q. Teixeiro, A. Larsson, and T. Suhara, "Deep-etched distributed Bragg reflector lasers with curved mirrors. Experiments and modeling," *IEEE J. Quantum Electron.*, vol. 37, no. 6, pp. 752–761, Jun. 2001, doi: 10.1109/3.922772.

[53]   A. Melloni and M. Martinelli, "Synthesis of direct-coupled-resonators bandpass filters for WDM systems," *J. Light. Technol.*, vol. 20, no. 2, pp. 296–303, Feb. 2002, doi: 10.1109/50.983244.

[54]   M. Kaur and S. Dewra, "Investigation of Photonic Integrated Circuits with Low-Loss Bragg Gratings," *J. Opt. Commun.*, vol. 41, no. 3, pp. 229–233, Apr. 2020, doi: 10.1515/joc-2017-0177.

[55]   A. Melloni *et al.*, "Tunable Delay Lines in Silicon Photonics: Coupled Resonators and Photonic Crystals, a Comparison," *IEEE Photonics J.*, vol. 2, no. 2, pp. 181–194, Apr. 2010, doi: 10.1109/JPHOT.2010.2044989.

[56]   A. F. Abdelshafy, M. A. K. Othman, D. Oshmarin, A. T. Almutawa, and F. Capolino, "Exceptional Points of Degeneracy in Periodic Coupled Waveguides and the Interplay of Gain and Radiation Loss: Theoretical and Experimental Demonstration," *IEEE Trans. Antennas Propag.*, vol. 67, no. 11, pp. 6909–6923, Nov. 2019, doi: 10.1109/TAP.2019.2922778.

[57]   J. Scheuer and O. Weiss, "The Serpentine Optical Waveguide: engineering the dispersion relations and the stopped light points," *Opt. Express*, vol. 19, no. 12, p. 11517, Jun. 2011, doi: 10.1364/OE.19.011517.